The CatWISE Preliminary Catalog: Motions from *WISE* and *NEOWISE* Data

Peter R. M. Eisenhardt,[1] Federico Marocco,[1, 2, *] John W. Fowler,[3] Aaron M. Meisner,[4, †]

J. Davy Kirkpatrick,[2] Nelson Garcia,[2] Thomas H. Jarrett,[5] Renata Koontz,[6]

Elijah J. Marchese,[6] S. Adam Stanford,[7] Dan Caselden,[8] Michael C. Cushing,[9]

Roc M. Cutri,[2] Jacqueline K. Faherty,[10] Christopher R. Gelino,[2] Anthony H. Gonzalez,[11]

Amanda Mainzer,[1] Bahram Mobasher,[12] David J. Schlegel,[13] Daniel Stern,[1]

Harry I. Teplitz,[2] and Edward L. Wright[14]

[1]*Jet Propulsion Laboratory, California Institute of Technology, 4800 Oak Grove Drive, M/S 169-327, Pasadena, CA 91109, USA*

[2]*IPAC, Mail Code 100-22, California Institute of Technology, 1200 E. California Blvd., Pasadena, CA 91125, USA*

[3]*230 Pacific St., Apt. 205, Santa Monica, CA 90405, USA*

[4]*National Optical Astronomy Observatory, 950 N. Cherry Ave., Tucson, AZ 85719, USA*

[5]*Department of Astronomy, University of Cape Town, Private Bag X3, Rondebosch, 7701, South Africa*

[6]*University of California, Riverside, 900 University Ave, Riverside, CA 92521, USA*

[7]*Department of Physics, University of California Davis, One Shields Avenue, Davis, CA 95616, USA*

[8]*Gigamon Applied Threat Research, 619 Western Avenue, Suite 200, Seattle, WA 98104, USA*

[9]*Department of Physics and Astronomy, University of Toledo, 2801 West Bancroft St., Toledo, OH 43606, USA*

[10]*Department of Astrophysics, American Museum of Natural History, Central Park West at 79th Street, NY 10024, USA*

[11]*Department of Astronomy, University of Florida, 211 Bryant Space Center, Gainesville, FL 32611, USA*

[12]*University of California, Riverside, 900 University Ave, Riverside, CA 92521*

[13]*Lawrence Berkeley National Laboratory, Berkeley, CA, 94720, USA*

[14]*Department of Physics and Astronomy, UCLA, 430 Portola Plaza, Box 951547, Los Angeles, CA 90095-1547, USA*

Corresponding author: Peter R. M. Eisenhardt.
Peter.R.Eisenhardt@jpl.nasa.gov

Submitted to Astrophysical Journal Supplement

ABSTRACT

CatWISE is a program to catalog sources selected from combined *WISE* and *NEO-WISE* all-sky survey data at 3.4 and 4.6 μm (W1 and W2). The CatWISE Preliminary Catalog consists of 900,849,014 sources measured in data collected from 2010 to 2016. This dataset represents four times as many exposures and spans over ten times as large a time baseline as that used for the AllWISE Catalog. CatWISE adapts AllWISE software to measure the sources in coadded images created from six-month subsets of these data, each representing one coverage of the inertial sky, or epoch. The catalog includes the measured motion of sources in 8 epochs over the 6.5 year span of the data. From comparison to *Spitzer*, the SNR=5 limits in magnitudes in the Vega system are W1=17.67 and W2=16.47, compared to W1=16.96 and W2=16.02 for AllWISE. From comparison to *Gaia*, CatWISE positions have typical accuracies of $50\,\mathrm{mas}$ for stars at W1=$10\,\mathrm{mag}$ and $275\,\mathrm{mas}$ for stars at W1=$15.5\,\mathrm{mag}$. Proper motions have typical accuracies of $10\,\mathrm{mas\,yr^{-1}}$ and $30\,\mathrm{mas\,yr^{-1}}$ for stars with these brightnesses, an order of magnitude better than from AllWISE. The catalog is available in the WISE/NEOWISE Enhanced and Contributed Products area of the NASA/IPAC Infrared Science Archive.

Keywords: catalogs, infrared:stars, proper motions, brown dwarfs

1. INTRODUCTION

NASA's *Wide-field Infrared Survey Explorer* mission (*WISE*; Wright et al. 2010) revealed iconic objects, including the first Earth Trojan asteroid (Connors et al. 2011), the closest and coolest brown dwarfs (Luhman 2013, 2014), and the most luminous galaxy yet found in the Universe (Tsai et al. 2015). These discoveries were made using two or more infrared coverages of the sky (or epochs)

---

* NASA Postdoctoral Program Fellow
† Hubble Fellow

obtained from January 2010 to February 2011. Each epoch typically consists of a dozen exposures per band taken within two days at a given position. The satellite was reactivated as *NEOWISE* and resumed searching for near-Earth objects in December 2013 (Mainzer et al. 2014), and has continued to cover the sky every six months since then.

In November 2013, the AllWISE release (Cutri et al. 2013) made available to the community an atlas from coadding the two dozen exposures per position from the initial year of WISE surveying, and a catalog of source fluxes and positions measured from those exposures. With at least two epochs per inertial position, AllWISE also provided motion estimates, and became the definitive catalog in the WISE bandpasses. Each year, *NEOWISE* releases the individual exposures from the reactivated survey (Cutri et al. 2015), corresponding to two additional epochs. With the 2019 April 10 *NEOWISE* release, exposures from 12 epochs are now available. Meisner et al. (2018a) used unWISE processing (Lang 2014) to produce an image atlas which combines the 2010 and 2011 data used for AllWISE with the 2013 through 2016 *NEOWISE* data. An obvious next step is to catalog the sources revealed in these combined exposures.

The unWISE Catalog (Schlafly et al. 2019) uses a crowded-field point-source photometry code called "crowdsource" to do this, measuring source fluxes and positions in the coadded image, with the measurements at 3.4 μm (W1) and 4.6 μm (W2) carried out independently. In contrast, CatWISE has adapted AllWISE software to produce a full-sky catalog of sources selected simultaneously in both W1 and W2, and also provides motion estimates. For the CatWISE Preliminary Catalog described in this paper, sources were selected from the ensemble of 8 epochs of *WISE* and *NEOWISE* data from Meisner et al. (2018a, the "full coadd"), and the least-squares best-fit solution for point source flux, position and motion were determined from measurements on the individual "epoch coadd" images (Meisner et al. 2018c) rather than individual exposures, to reduce computational cost. Because the total time spanned by CatWISE epochs at a given inertial position is over 6 years, compared to a typical value of 6 months for AllWISE, the CatWISE motion estimates are far more accurate. This in addition to the greater depth of the CatWISE catalog relative to AllWISE are being used to extend the census of the coldest brown dwarfs in the solar neighborhood and enable definitive measurement

of the form of the low-mass end of the star formation process (Kirkpatrick et al. 2019). Figure 1 illustrates an example of the potential of CatWISE to progress in this area.

In §2 of this paper we summarize relevant aspects of the *WISE* and *NEOWISE* mission phases. §3 describes the CatWISE processing steps. §4 assesses the astrometric and photometric performance of CatWISE using comparisons to *Gaia* and *Spitzer* data. §5 provides some initial examples of science results enabled by CatWISE, and §6 provides information on accessing CatWISE data products. Appendices provide additional information on CatWISE column entries, cautions on known issues in the CatWISE Preliminary Catalog, and details on how positions were combined from alternating survey scan directions (§2). The CatWISE website is https://catwise.github.io.

2. OBSERVATIONS

WISE was launched on 2009 December 14, with its 40-cm telescope cooled to 12 K by an outer cryostat tank, and the W1 and W2 detectors operated at 32 K. The 12 and 22 μm (W3 and W4) detectors were cooled to 7.8 K by an inner cryostat tank. Both tanks were filled with frozen hydrogen. The cryostat cover was ejected and the first images obtained on 2009 December 31, and science survey data were taken starting on 2010 January 7.

WISE uses dichroics to image the same 47×47 arcmin region of sky simultaneously in all bands using 1024×1024 pixel arrays with $2\rlap{.}''75$ pixels, and obtaining exposures every 11 seconds. The duration of each W1 and W2 exposure is 7.7 seconds due to readout time and scan mirror settling, and discarding the initial readout.

The Sun-synchronous polar *WISE* orbit was designed to precess so that the satellite stays over the Earth's terminator. The basic *WISE* survey strategy is to point near the zenith, scanning at the orbital rate along lines of ecliptic longitude, with the image motion compensated by a scan mirror that flies back for the start of each exposure. The precession rate sweeps across the imaging field of view in approximately 12 orbits (less than one day) near the ecliptic, although the detailed survey strategy extends this time to more than a day. Because images are obtained on both sides of the orbit, the same region of inertial sky is covered every six months, with the direction of the survey scans
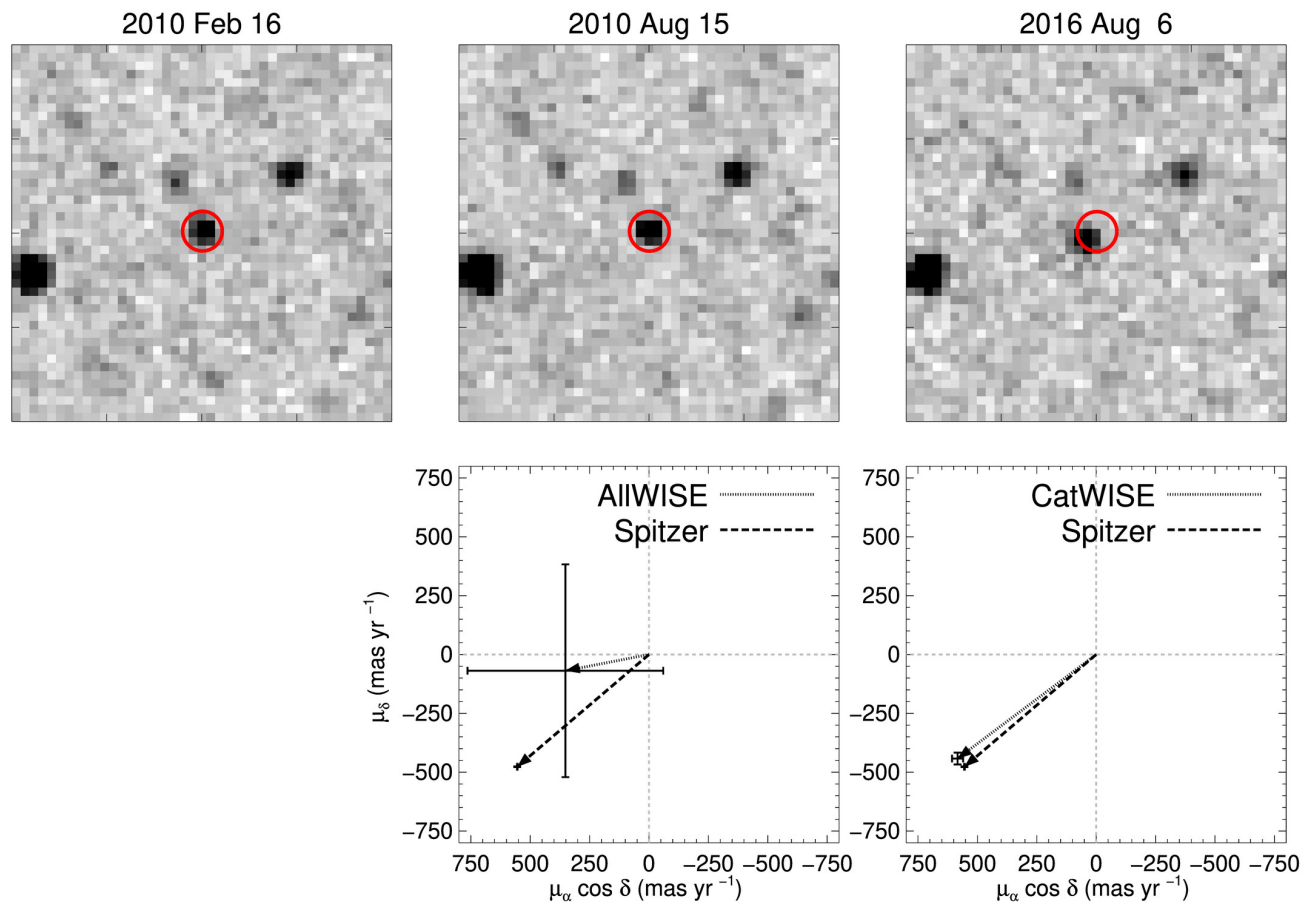
Figure 1. (top) Proper motions that are insignificant in AllWISE become obvious with the increased time baseline of CatWISE. Discovered via its color in WISE data (Gelino et al. (2011); Kirkpatrick et al. (2011)), WISEA J161441.47+173935.4 is a T9 brown dwarf at 10 pc with a proper motion of $\mu_\alpha = 554.5 \pm 1.2$ mas yr^{-1}, $\mu_\delta = -476.7 \pm 1.2$ mas yr^{-1} as determined by *Spitzer* (Kirkpatrick et al. 2019). With a 6-month baseline, AllWISE (top left and center) measures a motion consistent with zero ($\mu_\alpha = 352 \pm 412$ mas yr^{-1}, $\mu_\delta = -69 \pm 452$ mas yr^{-1}; bottom center), while with the inclusion of *NEOWISE* data from 2016 (top right), the corresponding source in the CatWISE Preliminary Catalog (CWISEP J161441.63+173933.7) has a highly significant motion ($\mu_\alpha = 583.6 \pm 23.5$ mas yr^{-1}, $\mu_\delta = -442.0 \pm 25.0$ mas yr^{-1}; bottom right) consistent with the *Spitzer* values. The top panels show $2' \times 2'$ cutouts in W2 centered on the *WISE* position of the source at the first epoch, marked in all 3 epochs by a red circle.

alternating between ascending and descending in ecliptic latitude. CatWISE processes ascending and descending scans separately for source measurement.
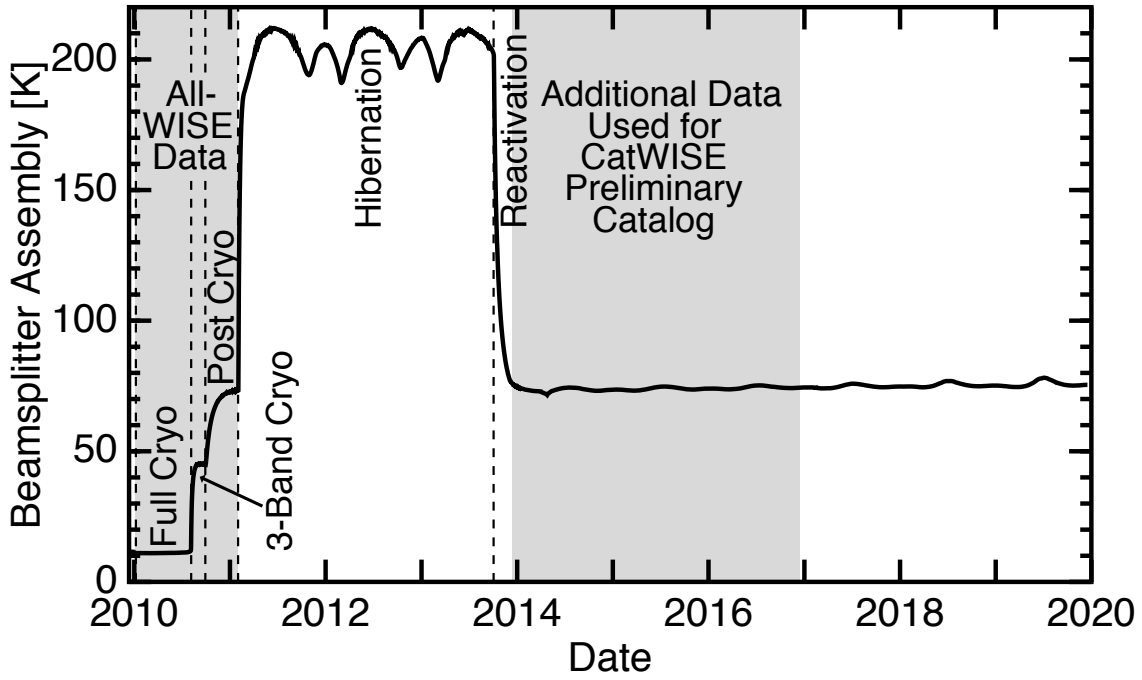
Figure 2. Temperature of the *WISE* beamsplitter assembly vs. date. This temperature is close to that of the telescope and W1 and W2 detectors. Dashed lines indicate the transitions from full cryogenic to 3-band cryogenic phases, to the post-cryogenic phase, and to the start of hibernation and reactivation. Grey shading indicates the date ranges of data used for the CatWISE Preliminary Catalog. AllWISE included only the left portion of the shaded range.

The fully cryogenic survey continued until the hydrogen in the outer tank evaporated on 2010 August 6, exceeding the 7-month cryogen lifetime requirement and covering the sky 1.2 times (Figure 2). WISE then surveyed an additional 30% of the sky during its 3-Band (W1, W2, and W3) cryogenic phase, with the W3 detector operating at reduced sensitivity. After the cryogen in both tanks was exhausted on 2010 September 29, the post-cryogenic *NEOWISE* survey (Mainzer et al. 2011) in W1 and W2 began, as the telescope and detectors warmed to ~ 73 K. Surveying continued until 2011 February 1, completing a second pass over the sky in W1 and W2, after which the satellite was placed into hibernation. In September 2013, the spacecraft was brought out of hibernation, where it had equilibrated at ~ 200 K due to thermal radiation from the Earth, and renamed *NEOWISE*. On 2013

December 13, with the telescope and detectors passively cooled below 76 K, *NEOWISE* resumed surveying the sky every 6 months in W1 and W2 (Mainzer et al. 2014).

The CatWISE Preliminary Catalog is based on the combination of W1 and W2 exposures in the two sky coverages used for the AllWISE data release (Cutri et al. 2013) and in the six additional sky coverages from the 2017 *NEOWISE* data release. For PSF purposes (§3.2), we use MJD 55480 (2010 Oct. 11) as the dividing point between cryogenic and post-cryogenic data. The average observation date is closer to MJD 56700 (2014 Feb. 12), which we adopt as the epoch for reporting positions when solving for source motion in the Preliminary Catalog. Source positions, whether incorporating source motion or not, are given in the equinox J2000 coordinate frame. Magnitudes in the catalog and throughout this paper are on the Vega system.

3. CATWISE PROCESSING

CatWISE adapts the AllWISE pipeline to detect and measure source fluxes in the combined WISE and *NEOWISE* images provided by unWISE. A full description of the AllWISE pipeline is provided in Cutri et al. (2013).

CatWISE processing works in the atlas tile footprint established by the WISE All-Sky Release, dividing the inertial sky into 18,240 overlapping square images (tiles), each approximately 1.56° on a side, aligned with the local right ascension and declination. Except for the "primary flagging" step (§3.6), processing steps were carried out independently on each tile. For the Preliminary Catalog, CatWISE uses the full depth unWISE coaddition of 8 epochs (Meisner et al. 2018a), and the 8 individual unWISE epoch coadds (Meisner et al. 2018c, after astrometric modifications described in §3.1). The full depth coadds and the PSF (§3.2) were used to create detection images. Sources were detected in these images (§3.3), while source properties were determined from measurements on the epoch coadds, treating ascending and descending epochs (§2) separately for most tiles and then merging the results (§3.4). Potential artifacts affecting the sources were identified (§3.5), and sources with multiple measurements because they were in the tile overlap region were flagged to indicate which set of measurements should be used (§3.6). Finally, sources were selected for inclusion in the catalog or reject files (§3.7). We describe these steps in more detail below.

3.1. *unWISE Coadds*

The coadded images in the atlas released with the AllWISE (and All-Sky) Catalogs were primarily intended to facilitate source detection, and for this reason they are convolved with the WISE PSF. The unWISE coadds retain the resolution of individual WISE exposures. To reduce differences from the AllWISE processing approach, for source detection (§3.3) in the CatWISE Preliminary Catalog, we convolved the masked version (Lang 2014) of the full-depth unWISE coadds Meisner2018a with the PSF (§3.2). For source measurement (§3.4) we used the masked version of the unWISE epoch coadds (Meisner et al. 2018c) without convolution.

An adjustment was made to the world coordinate system (WCS) for the pre-hibernation unWISE epoch coadds. Although all of the released individual exposures are tied to 2MASS (Skrutskie et al. 2006), the individual pre-hibernation exposures released for AllWISE are not on the same astrometric system as the individual post-hibernation exposures released for *NEOWISE*. The *NEOWISE* images include corrections for the motions of the 2MASS reference stars, as does the AllWISE Catalog (see §V.2.b of the AllWISE Explanatory Supplement; Cutri et al. (2013)), but the released pre-hibernation images do not include those corrections. A table of corrections for these images exists, however[1], and these corrections were applied to the unWISE input, making the astrometric system of the pre-hibernation epoch coadds consistent with those from the post-hibernation epoch coadds.

3.2. *Point Spread Function (PSF)*

The *WISE* and *NEOWISE* PSFs have been well characterized at the individual exposure level, but CatWISE works with coadded images rather than individual exposures, so PSFs appropriate for these coadded images are needed. The W1 and W2 PSFs vary with position in the focal plane, and changed somewhat between the cryogenic and post-cryogenic phases of the mission, particularly for W1. The PSFs are also asymmetric, with an orientation that is fixed with respect to the focal plane, but the focal plane orientation with respect to equatorial coordinates varies between exposures. The focal plane orientation also flips every six months because at a given inertial location the survey scan

---

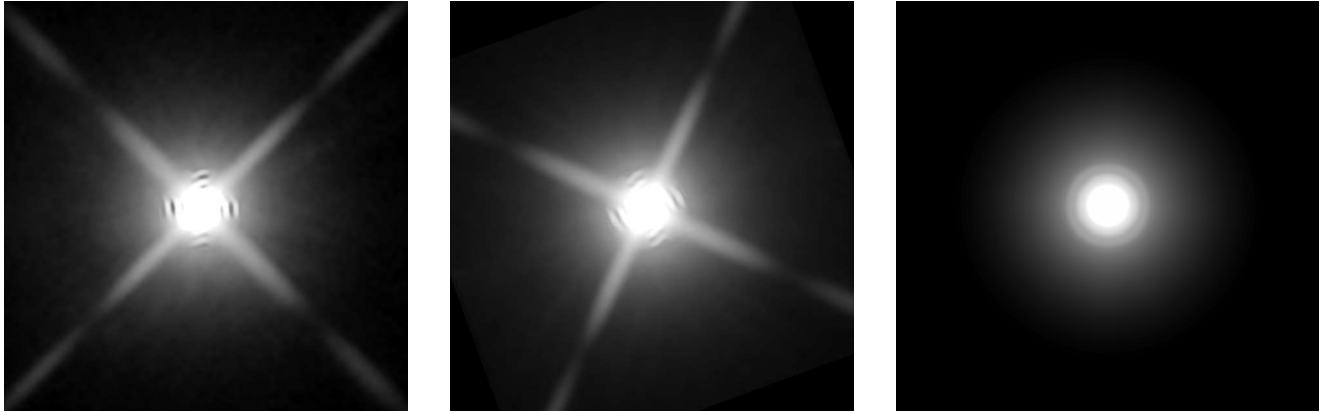[1] http://wise2.ipac.caltech.edu/docs/doc_tree/sis/rex19

Figure 3. *Left*: The "basic" (averaged over focal plane position) post-cryogenic PSF model for W1. The grey scale uses a log stretch from 1% to 99% of the peak value. The model extends to $\pm 110''$. *Center*: The ascending scan W1 PSF for tile 1497p015 after averaging over cryogenic and post-cryogenic epochs, and a PA range from 199.93° to 200.56°. This is illustrative of the type of PSF used by CatWISE for source measurement, with the exception of 50 tiles near the ecliptic poles. *Right*: The W1 PSF averaged over all scans for tile 0890m667, which includes the south ecliptic pole and all PAs. This is illustrative of the type of PSF used by CatWISE for source measurement for 50 tiles near the ecliptic poles.

direction alternates between ascending and descending in ecliptic latitude (§2). CatWISE addressed these issues as follows.

A 9×9 grid over the focal plane of cryogenic phase model PSFs and their uncertainties, $8\times$ oversampled relative to *WISE* pixels and covering 220" on a side, is provided in §IV.4.c.iii.1 of the *WISE* All-Sky Explanatory Supplement (Cutri et al. 2012). The post-cryogenic PSFs used for *NEOWISE* are given in §IV.2.b.i of the NEOWISE Explanatory Supplement (Cutri et al. 2015). Since many focal plane positions contribute to each source in the coadded images, CatWISE averaged these model PSFs, weighted only by their partition sizes in the 9×9 grid. The uncertainty in the averaged PSF was taken to be the root sum square of two terms: the root mean square of the individual grid PSF uncertainties divided by $\sqrt{N-1}$ where N is the 81 PSF's, and the standard deviation of the grid PSF's about the averaged PSF. Figure 3 (left) shows the resulting focal plane average post-cryogenic PSF model for W1. An analogous focal plane average cryogenic PSF was created for W1, as well as average cryogenic and post-cryogenic PSFs for W2. These are referred to below as the "basic" PSFs.
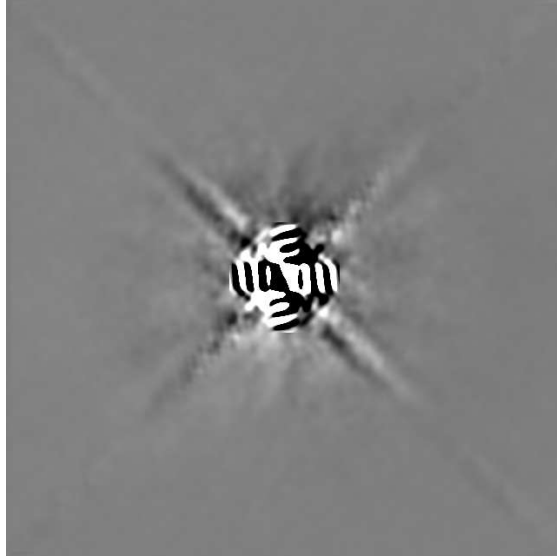
Figure 4. Difference image of W1 post-cryogenic PSFs in ascending vs. descending scans. The image extends to $\pm 110''$.

As can also be seen in the AllWISE PSF's plotted in Figure 1 of Lang, Hogg, & Schlegel (2016), the PSFs contain fine structure in the core that is qualitatively consistent with the expected diffraction pattern for WISE. This structure is not rotationally symmetric. Figure 4 shows the difference between ascending and descending orientations of the W1 post-cryogenic PSF. The bright and dark stripes in and around the core correspond to variations of roughly 25% of the peak of the PSF. The center of the PSF is the most crucial region for position estimation, so inaccuracies in this part of the PSF have serious consequences for astrometry, as well as photometry.

These structures are not due to misalignment of the ascending and descending PSF's, which would need to be $\sim 1''\!.0$ to account for the features – far greater than the difference in astrometry from the ascending vs. descending PSF's. For example, the median difference in source astrometry for tile 0895p227 (where ecliptic longitude and right ascension align) was 26.5 mas in ecliptic longitude, and 0.0 mas in ecliptic latitude. With the PSF's intentionally swapped, these values became -1216.0 mas in longitude and 633.6 mas in latitude. Over the sky, the tile median differences using the correct PSF's are distributed with a median value of 78.1 mas and $\sigma = 33$ mas in ecliptic longitude, and -14.4 mas and $\sigma = 16$ mas in ecliptic latitude.

The structure revealed here has no impact on the measurements carried out by the *WISE* and *NEOWISE* projects, because those measurements were made (and continue to be made) on individual exposures. The PSF structure is captured in the models, and the PSF orientation is always the same in the focal plane. This is not the case for CatWISE, which uses coadds in place of individual *WISE* exposures. The coadded image tile orientation is aligned with the local equatorial coordinates. Therefore CatWISE rotated the basic PSFs by an appropriate set of position angles (PAs) between focal plane and equatorial coordinates for each image tile.

The coadded images were assembled from individual exposures with a range of PA values, so histograms of exposure PA values were constructed for each tile, using a bin width of 0.1 degrees. Separate histograms were constructed for ascending vs. descending and cryogenic vs. post-cryogenic exposures. The basic PSF was rotated by each PA bin center value and these rotated PSFs averaged together with weights equal to the histogram bin count. Those averages were then combined for each tile with weights given by the number of corresponding cryogenic and post-cryogenic exposures to make ascending and descending PSFs for each tile.

Tiles in the vicinity of the ecliptic poles have large PA ranges, and so the tile PSF becomes very smeared (see Figure 3, right). For the 50 tiles nearest the ecliptic poles (listed in Table 1), the ascending and descending PSFs were averaged together, weighted by the number of ascending and descending exposures.

The description above applies to the PSF's used by CatWISE for source measurement. For the detection step in the Preliminary Catalog (§3.3), PSF's analogous to the measurement PSF's of the 50 tiles nearest the ecliptic poles were created for every tile, but with $4\times$ oversampling relative to the unWISE images, rather than the $8\times$ oversampling of the measurement PSF's. These detection PSF's were made by resampling the central portion of the weighted average of ascending and descending PSF's for that tile. The detection PSF's have 27×27 pixels with each pixel spanning $0\rlap{.}''6875$, i.e. covering an area of $18\rlap{.}''5625$ on a side (6.75 native WISE pixels).

Table 1. Tiles Processed Using a Single PSF per Band

RA range in decimal degrees of tiles in column				
79.1:87.9	89.0:95.7	96.2:264.2	265.0:272.1	272.6:280.8
0791m682	0890m667	0962m697	2650p681	2726p651
0803m652	0891m637	0964m667	2656p651	2729p681
0830m682	0908m652	0978m652	2672p666	2741p636
0837m697	0909m682	0988m682	2675p636	2746p666
0838m652	0920m697	1002m667	2679p696	2761p651
0853m667	0924m637	2610p681	2690p681	2762p696
0858m637	0927m667	2621p651	2691p651	2769p681
0870m682	0943m652	2635p666	2708p636	2783p666
0873m652	0949m682	2637p696	2709p666	2796p651
0879m697	0957m637	2642p636	2721p696	2808p681

3.3. *Detection*

Source detection for the CatWISE Preliminary Catalog was done simultaneously in W1 and W2 with the Multiband Detection (MDET; Marsh & Jarrett 2012) and Image Co-addition with Optional Resolution Enhancement (ICORE) software (Masci 2013) used in the WISE pipeline, following the process described in §IV.4.b.iii.1 of the WISE All-Sky Explanatory Supplement (Cutri et al. 2012). The detection PSF's in each band were used as matched filters to generate images which are optimal for detection of isolated point sources in that band. ICORE generated the convolution (or more accurately, the cross-covariance) of the PSF with the full-depth unWISE coadd, resampling the 2048×2048 $2\rlap{.}''75$ pixel unWISE coadds to the 4095×4095 $1\rlap{.}''375$ pixel detection image format employed by MDET for WISE. The resampling was done using nearest-neighbor interpolation into a temporary finer grid matching the PSF grid, before being down-sampled to the output pixel size. Similarly, ICORE created uncertainty images from the detection PSF's and the unWISE "std" images, which are the standard deviation of the individual exposures that comprise the unWISE full-depth

coadds. MDET then subtracted a local background from each ICORE image using a 21×21 pixel median filter, normalizing the result by the ICORE uncertainty image. To account for confusion noise, the uncertainties were augmented by the root-sum-square of the estimated variance of the ICORE image from the local background. Finally, MDET generated a detection image from these normalized and background-subtracted ICORE images by summing the two bands in quadrature, identifying as sources local maxima (pixels with larger values than their neighbors) that exceeded a specified detection threshold.

As was done for WISE, the detection threshold was set at an estimated source reliability of $\sim 50\%$. AllWISE, with two sky coverages, selected a threshold of 2.4, compared to 3.5 used for the single coverage WISE All-Sky Release. For CatWISE we estimated the threshold based on comparison to deeper *Spitzer* data from the SERVS (Mauduit et al. 2012) and S-COSMOS (Sanders et al. 2007) programs. These programs have a source density of $\sim 100,000$ deg^{-2}, so with the matching radius of $2\rlap{.}''5$ the chance of a spurious match is not trivial (15%), but still well below the 50% criterion for the detection threshold. The estimated threshold varied from 1.7 in the COSMOS field to 2.6 in the Lockman Hole, and a value of 1.8 was selected for the Preliminary Catalog.

At the high source densities typical for CatWISE in coadds of ~ 100 or more individual WISE exposures, this matched filter detection methodology yields an asymptotic number of $\sim 60,000$ detected sources per tile for the Preliminary Catalog (or $\sim 25,000$ deg^{-2}, Figure 5) and hence becomes incomplete, particularly in W1. The detected source density declines slightly in the Galactic plane, for reasons not well understood at present. The limiting source density corresponds to an exclusion radius of 13". This is similar to the decline in sources separated by less than 10" shown in Figure 27 of §VI.2.c.iv in the WISE All-Sky Explanatory Supplement (Cutri et al. 2012), so is likely a consequence of the source detection methodology used in the WISE pipeline. Schlafly et al. (2019) present an alternative approach ("crowdsource") which results in higher detected source densities, but does not provide motion estimates. We are using the Schlafly et al. (2019) catalog as the detection list for an updated version of the CatWISE catalog that is expected to be available in 2020. The completeness and reliability of the CatWISE Preliminary Catalog are discussed further in §4.1.
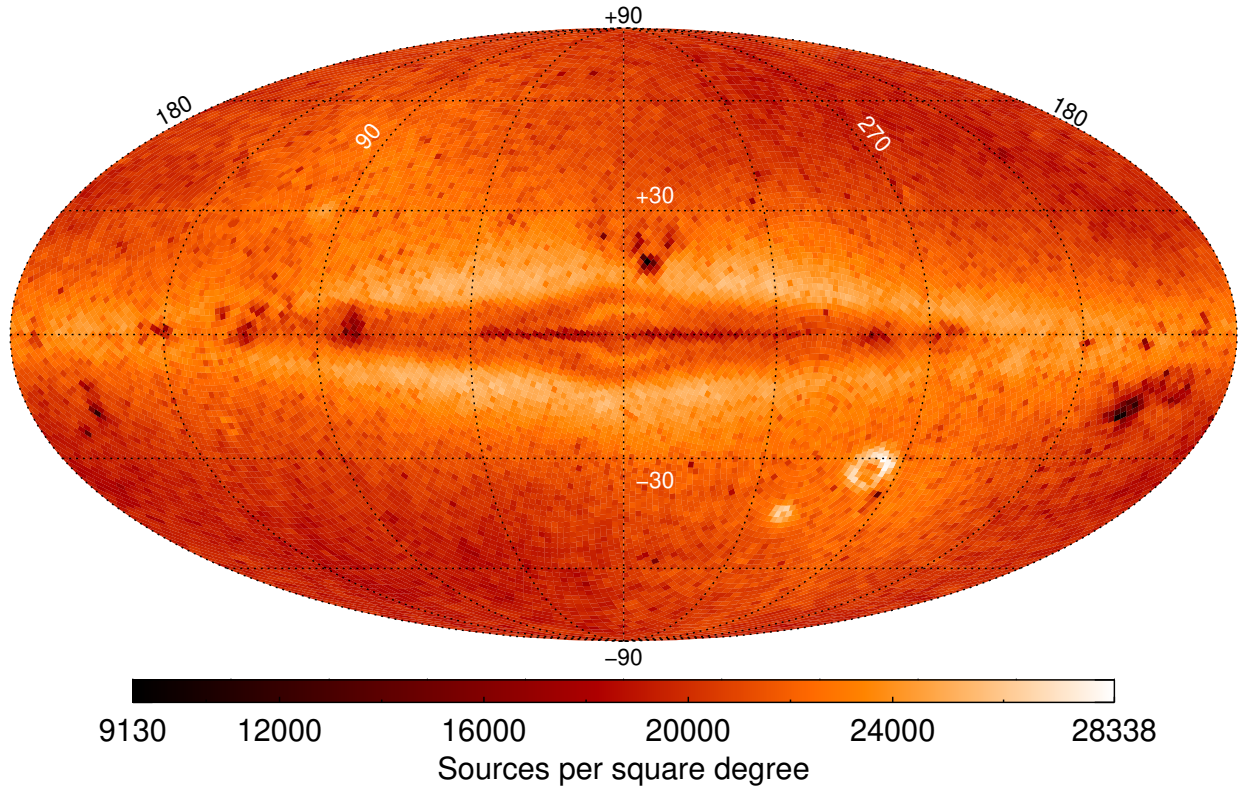
Figure 5. Map of CatWISE Preliminary Catalog source density in Galactic coordinates.

3.4. *Source Measurement*

Source photometry, astrometry, and motion estimation for CatWISE use an adapted version of the WPHOT software developed for the AllWISE pipeline. WPHOT carries out point-source extraction, solving for both photometry and astrometry simultaneously. Source positions detected in each coadded tile image were propagated to individual exposures, and the flux and χ^2 evaluated from fitting the PSF. The source position and flux were refined by searching for a local minimum in χ^2. For AllWISE, a linear motion was also solved for, based on the observation time of the images.

CatWISE did not have the computational resources to perform the source fitting on all of the many hundreds of individual exposures that contribute to a coadded tile image. Because the 12 exposures for a given inertial position in each sky coverage are obtained within less than two days, the motions

of sources beyond the solar system can be assumed to be fixed for each sky coverage (or epoch). Therefore CatWISE ran WPHOT treating unWISE epoch coadd images as the individual images.

The other significant modification to the AllWISE WPHOT process implemented by CatWISE addressed the alternating scan direction of each epoch and hence varying PSF orientation. WPHOT was not designed to use a time-dependent PSF, but with 8 or more epoch coadd images per position, CatWISE elected to measure source properties with WPHOT separately for the groups of four or more epoch coadds in each of the two scan directions, and then merge the two results. This methodology was used for all but the 50 tiles nearest the ecliptic poles, listed in Table 1. For those tiles, a tile-specific average PSF over all epochs was used for both scan directions, and all epochs were processed together with WPHOT.

WPHOT performs PSF-fit photometry and astrometry assuming sources are inertially fixed (the "stationary fit"), and also searches for a solution assuming a linear motion with time (the "motion fit"). The χ^2 minimization fit can be performed at any location in the flux image. The goal of astrometry is to find the location at which χ^2 has a local minimum.

The stationary fit uses the gradient descent method to minimize the total χ^2 (i.e., the combined W1 and W2 χ^2) in the two-dimensional space of right ascension (α) and declination (δ). As one moves around in the space, χ^2 decreases and increases as the local flux distribution appears more or less like a point source. The (α, δ) where χ^2 is estimated to be minimal is the position assigned to the source, and the scale factor on the PSF that minimizes χ^2 there is the flux estimate. The value of χ^2 is recorded, as are the individual χ^2 for the W1 and W2 flux fits. Under certain conditions such as low coverage or negative fluxes, the gradient descent algorithm may be unable to compute estimates, in which case nulls are reported. Standard Gaussian error analysis provides uncertainties for (α, δ) and flux. The error model includes both PSF error and image flux error, and is discussed further in §3.4.1. More details on WPHOT are given in §IV.4.c.iii of the *WISE* All-Sky Explanatory Supplement (Cutri et al. 2012).

The model used for the motion solution replaces the single location of the stationary solution with locations along a linear function of time. The slopes of this line in the (α, δ) directions are the angular

motion rates (μ_α, μ_δ) in (α, δ). The motion fit minimizes the total χ^2 over the four-dimensional space of $(\alpha, \delta, \mu_\alpha, \mu_\delta)$. When the motion fit is based on both ascending and descending epochs, the motions will include parallax effects (see Kirkpatrick et al. 2014), and so they are not true proper motions. However, except for the 50 tiles near the ecliptic poles, CatWISE processed ascending and descending scans separately, so that the measured motions are close to true proper motions.

3.4.1. *Uncertainties*

WPHOT estimates uncertainties in photometry, position, and motion based on error propagation from uncertainty images corresponding to the PSF and exposure images. The PSF uncertainty images from *WISE* and *NEOWISE* appropriate to each PSF were combined using the methodology described in §3.2, and these dominate the uncertainties estimated for brighter stars ($\lesssim 12$ mag). For fainter sources ($\gtrsim 15$ mag) the exposure image (or for CatWISE, epoch image) uncertainties dominate. For these, the "std" unWISE images were used, which are the sample standard deviation at each pixel of the individual WISE exposures divided by $\sqrt{N - 1}$, where N is the number of exposures.

Reduced χ^2 values from the CatWISE PSF fitting measurements showed that the uncertainties needed adjustment. The PSF uncertainties were scaled down by 0.9 in W1 and 0.64 in W2 based on bright star reduced χ^2 values. Cryogenic PSF uncertainties for W1 were scaled down by an additional factor of 0.58. Based on faint star reduced χ^2 values, the image uncertainties were scaled up by 1.4 in W1 and 1.15 in W2, and those for pre-hibernation epochs were scaled up by additional factors of 1.1 in W1 and 1.05 in W2. The units of the unWISE images are Vega nanomaggies (nMgy), i.e. 0.306681 μJy for W1 and 0.170663 μJy for W2 (Wright et al. 2010), and a minimum value of 1 nMgy in W1 and 10 nMgy in W2 was also imposed on the image uncertainties.

The uncertainties for the 50 tiles near the ecliptic poles, which used averages of ascending and descending PSFs (§3.2) had somewhat different adjustments. For these tiles the PSF uncertainties were scaled up by 1.3 in W1, with no further adjustment for cryogenic values, and were left unchanged for W2. The image uncertainties were scaled up by 1.75 in W1 and 1.25 in W2, and those for pre-hibernation epochs were scaled up further by 1.1 in W1 and 1.05 in W2. A minimum value of 1 nMgy in W1 and 5 nMgy in W2 was imposed on the image uncertainties.

3.4.2. *Merging Measurements from Ascending and Descending Scans*

As noted earlier, for nearly all tiles two independent measurements were made, one extracted from epoch coadds constructed from ascending scans and one from descending-scan epochs. These were merged into a single source list as follows.

Sources were matched based on their identifier in the detected source list (§3.3). A small number of mismatches occurred because of active deblending in WPHOT. Active deblending inserts a new source (not from the detection program) into the fitting region if the χ^2 value exceeds a threshold and is reduced by the insertion by a minimum required amount. Full details may be found in §IV.4.c of the *WISE* All-Sky Explanatory Supplement (Cutri et al. 2012). Actively deblended sources have the same identifier as the parent source in the detection list. Because active deblending may proceed differently in the ascending and descending data, when the identifier was not unique, a nearest-match criterion was also applied. If the number of ascending sources did not equal the number of descending sources, the left over sources were discarded, leaving a one-to-one association list.

Corresponding parameters for each matched ascending-descending source pair were combined when the ascending and descending apparitions have non-null values (§3.4), otherwise the single non-null values (if any) were retained. Aperture magnitudes for the ascending and descending scans were measured from the same full-depth coadd, differing only slightly in the position of the aperture centers. Hence, the fluxes and flux uncertainties corresponding to the aperture magnitudes and their uncertainties were simply averaged without weighting. Positions were averaged using inverse-covariance weighting, with the averaging done in a local Cartesian projection consistent with the uncertainty representation. Additional details are provided in Appendix C. PSF-fit photometry was combined by averaging the flux values using inverse-variance weighting. This yields refined flux values and reduced uncertainties that are used to recompute the magnitudes, magnitude uncertainties, and signal-to-noise ratios.

3.5. *Artifact Flagging*

Bright stars create a variety of scattered light effects and electronic charge issues that require special handling by the software. These effects include scattered light halos, diffraction spikes, glints from off-frame bright stars, optical ghosting from internal reflections within the optical system, and charge persistence on the arrays. These can create false detections, hereafter called artifacts, or can contaminate detections of real, astrophysical sources. The goal of artifact flagging is to label spurious or affected sources so that the user can easily create source lists for which most of these problems are eliminated.

The CatWISE Preliminary Catalog employs two types of artifact flagging. One is the *cc_flags* values copied directly from AllWISE processing. If a source was found in either the AllWISE Catalog or Reject Table within $2\rlap{.}''75$ of a CatWISE source, its *cc_flag* was included in the entry for the CatWISE source; if no AllWISE source was found within this radius, then *cc_flags* contains a null value. For a CatWISE source having multiple AllWISE sources within the $2\rlap{.}''75$ radius, the most pessimistic value per band was retained, as described in §3.5.1. These *cc_flags* values indicate whether a source is likely to be spurious because it is dominated by an artifact (encoded as an upper-case letter) or is a real source contaminated by an artifact (encoded as a lower-case letter). Each of the four characters in *cc_flags* corresponds to artifacts in one of the four WISE bands, so the first two characters are most relevant for CatWISE, which does not include W3 or W4 data. The possibilities are "0" for no artifact or contamination, "D" or "d" for a diffraction spike, "H" or "h" for a scattered light halo, "O" or "o" for an optical ghost, or "P" or "p" for charge persistence. The *cc_flags* field conveys only the main features of the full artifact flag information contained in the AllWISE *w1cc_map*, *w1cc_map_str*, *w2cc_map*, and *w2cc_map_str* fields,[2] which are also provided in the CatWISE source entry. A more detailed description can be found in §IV.4.g of the *WISE* All-Sky Explanatory Supplement (Cutri et al. 2012).

---

[2] Note that the column descriptions for these fields in §II.1.a of the AllWISE Explanatory Supplement (Cutri et al. 2013) are incorrect. Corrected descriptions are provided in Appendix A.

The second type of artifact flag is called ab_flags, which was determined for every CatWISE source and is based on artifact flagging images provided by unWISE (unWISE bit masks; Meisner et al. 2019a). The ab_flags do not attempt to distinguish between an outright artifact and a real astrophysical source that suffers from some level of artifact contamination, but are set so that only egregious artifacts more likely to be spurious detections are flagged. By analogy with cc_flags, the ab_flags thus contain only upper-case letters "D", "H","O", or "P" or the value "0". Furthermore, because the CatWISE data deal only with W1 and W2 data, the ab_flags values are only two characters long. Additional details are given in §3.5.2.

Figure 6 shows examples of both types of artifact flags. These cc_flags and ab_flags values should be regarded as two different yet complementary methods for tagging sources of special concern to the user. As described in § IV.4.g of the *WISE* All-Sky Explanatory Supplement (Cutri et al. 2012), the cc_flags are known to overflag; their purpose is to produce a reliable catalog of source extractions free of contamination by artifacts, but they do so at the expense of completeness. AllWISE cc_flags are not available for sources detected only in CatWISE, so requiring a source to have "0" in its cc_flags entry again emphasizes reliability over completeness. In contrast the ab_flags, which are available for every CatWISE source, are used to tag only the more egregious artifacts, thereby emphasizing completeness, albeit at the expense of reliability. Users of the CatWISE data products can thus query against these two sets of artifact flags to best fit their needs.

3.5.1. *Setting the cc_flags Values When There are Multiple Matches*

The values of cc_flags were taken directly from a join of the AllWISE Point Source Catalog and Reject Table. When more than one of these AllWISE sources matched to within $2\rlap{.}''75$ of a CatWISE source, the band-by-band cc_flags value of the CatWISE source was determined as follows. If there was an upper-case letter for any matching source, it took precedence over any lower-case letter. The letter "D" is the highest priority followed, in order, by "P", "H", and "O". If there were no upper-case letters for any matching source, lower-case letters had the next highest priority, in the same order ("d", "p", "h", and "o"). If all matching sources had a value of "0" in that band, then "0" was used.
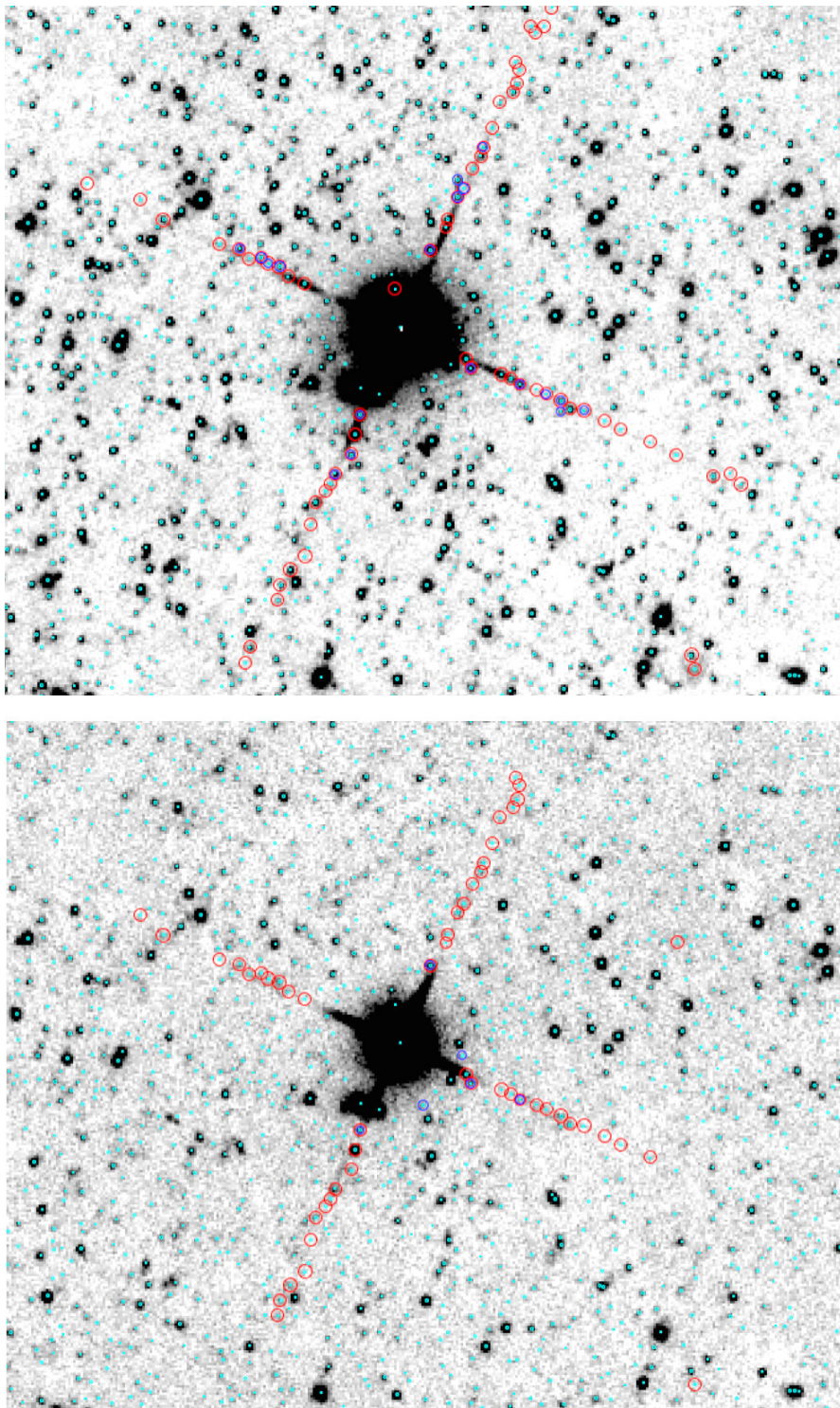
Figure 6. Example artifact flags for $16.5' \times 13.0'$ cutouts in W1 (top) and W2 (bottom) from the tile 1497p015. Detected CatWISE sources are shown by the small cyan circles. Sources with upper-case cc_flags are marked with large red circles, and sources labeled as artifacts by ab_flags are marked in medium-sized blue circles.

For the binary bit encoding of AllWISE artifacts given by *w1cc_map* and *w2cc_map*, when there was more than one AllWISE match to a CatWISE source, a logical 'OR' was performed over all the matches for each bit. The *w1cc_map_str* and *w2cc_map_str* values were then constructed using the priority rules given in the previous paragraph.

3.5.2. *Translating the unWISE Bit Mask Values to ab_flags*

The unWISE bit mask values at the (x,y) pixel location of the source were used to set the value of *ab_flags*, as shown in Table 2, where we use the prefix "b" to indicate specific unWISE mask bits in column 3. Bits 0–3 and 7–8 are related to a nearby bright star; bits 11, 12, 25, and 26 indicate optical ghosts; bits 13–20 flag charge persistence; bits 23 and 24 mark halos; and bits 27–30 are for diffraction spikes. The checks against bits 21 and 22 are to ensure that the bright star is not flagged by its own diffraction spikes or scattered light halo. A complete description of the unWISE mask bits is given in Meisner et al. (2019a).

Table 2. Logic Used in Converting unWISE Bitmask Values to *ab_flags* Values

Value	Band	Logic
"D"	W1	b0 or b1 or b7 or b27 or b29 but only if not b21
$\cdots$	W2	b2 or b3 or b8 or b28 or b30 but only if not b22
"H"	W1	b23 but only if not b21
$\cdots$	W2	b24 but only if not b22
"O"	W1	b25 or b26
$\cdots$	W2	b11 or b12
"P"	W1	b13 or b14 or b17 or b18
$\cdots$	W2	b15 or b16 or b19 or b20

In addition to the *ab_flags* field, the CatWISE catalog includes fields with detailed artifact flag information (*w1ab_map*, *w1ab_map_str*, *w2ab_map*, and *w2ab_map_str*) for each source, analogous to the similar fields providing detailed artifact information related to *cc_flags*.

3.6. *Duplicate Source Measurements*

WISE tiles, and, therefore, unWISE coadds, overlap each other by $\sim 3'$ on the equator. As a result, sources appearing near the edge of a tile will also be measured in neighboring tiles. To remove these duplicate measurements we adopted the approach used by Schlafly et al. (2019). For each source in a tile, its coordinates were used to calculate the minimum distance to the edge of the tile. The same coordinates were used to calculate the minimum distance to the edge for all neighboring tiles, and the source was flagged as "primary" if these other minimum distances were all smaller.

3.7. *The CatWISE Preliminary Catalog*

With the necessary flagging in place, catalog generation could proceed. CatWISE Preliminary Catalog sources are required to:

1) be from the tile where that source is furthest from the tile edge (i.e. flagged as "primary," §3.6) and

2a) have W1 SNR ≥ 5 with no identified artifacts (a value of 0 in the left character of *ab_flags*) or

2b) have W2 SNR ≥ 5 with no identified artifacts (a value of 0 in the right character of *ab_flags*).

There are 900,849,014 sources that meet these criteria. The 167,831,546 sources that fail to meet these criteria go into the reject file for their tile. Individual tile reject files typically contain 8,000 sources, although near the celestial poles they can contain over 30,000 sources due to large tile overlap. There are 186 formatted columns of information about each source in the tile catalog files. Reject files have one additional column, indicating if the source is primary in its tile. Descriptions of most of the columns are available in §II.1.a of the AllWISE Explanatory Supplement (Cutri et al. 2013), and Appendix A provides additional information about CatWISE columns.

The individual Preliminary catalog and reject files for the 18,240 tiles were transferred to the NASA Infrared Science Archive (IRSA), where they were merged into the IRSA database. Four columns (with names in italics in Table 4) were removed from view by IRSA, for reasons explained in that Table. Information regarding access to the catalog is provided in §6.

CatWISE source designations should have the prefix CWISEP for objects in the CatWISE Preliminary Catalog, and CWISEPR for objects in the CatWISE Preliminary Reject Table. The designation for each source, based on its coordinates for the J2000 equinox following the IAU truncation convention and without the leading CWISEP or CWISEPR prefix, is given by the field *source_name* which is the first column in the files. For example, the quasar 3C 273 is CWISEP J122906.70+020308.6[3]

4. PERFORMANCE CHARACTERIZATION

The greatest potential for improvement of the CatWISE Preliminary Catalog over existing *WISE* catalogs is in providing more accurate motion measurements, due to the much longer time baseline compared to AllWISE. Hence, characterization has focused on astrometric properties of the Preliminary Catalog. Photometric depth is also improved due to the four times larger number of exposures than AllWISE. Characterization has emphasized comparison to external truth sets, using *Spitzer* for photometric comparisons including completeness and reliability, and *Gaia* for astrometric comparisons. We begin with the photometric assessments.

4.1. *Completeness and Reliability*

4.1.1. *Bright Sources*

CatWISE completeness and reliability for sources with W1 or W2 <8 mag were assessed using an updated version of the *WISE* Bright Star List (BSL) as a truth set. The list was generated by the *WISE* team for artifact flagging (see §4.4.g.vi in the *WISE* All-Sky Release Explanatory Supplement; Cutri et al. 2012). To avoid degradation of completeness or reliability due to missed matches for fast-moving sources, astrometric information for sources moving faster than $0\rlap{.}''275$ yr^{-1} was added to the

---

[3] The CatWISE Preliminary Catalog coordinates for 3C 273 are within $0\rlap{.}''011$ of the Gaia DR2 coordinates.

BSL to propagate the positions of such stars to the CatWISE epoch. Astrometric information was taken from *Gaia* DR2 (Gaia Collaboration et al. 2018; Lindegren et al. 2018) or, when not available (given *Gaia*'s known incompleteness for bright stars) from the *Hipparcos* main catalog (van Leeuwen 2007), the Luyten Half-Second catalog (Bakos et al. 2002), or the Gliese-Jahreiß catalog (Stauffer et al. 2010).

CatWISE completeness was determined as the percentage of sources that have astrometric matches in CatWISE as a function of BSL magnitude. Differential CatWISE reliability was determined as the percentage of sources that have astrometric matches in the BSL as a function of CatWISE magnitude. We used a relatively large matching radius of $5\farcs5$ (corresponding to two *WISE* pixels) to account for the poorer centroiding accuracy expected for highly saturated sources.

Figure 7 shows the results for completeness, compared to those from AllWISE. CatWISE achieves $\sim 99\%$ completeness in the BSL W1$\sim 5.5 - 8$ mag and BSL W2$\sim 5 - 8$ mag ranges, slightly lower than AllWISE. For reasons that we have not investigated, CatWISE completeness drops for brighter stars, falling to $\sim 50\%$ by W1~ 4.3 mag and W2~ 3.6 mag. AllWISE completeness remains above 90% even for stars as bright as 0.25 mag, making it preferable to CatWISE for investigations of the brightest stars.

CatWISE reliability is $\sim 99\%$ for W1$\sim 4.8 - 8$ mag and W2$\sim 4.5 - 8$ mag, somewhat better than AllWISE, as can be seen in Figure 8. (For sources without artifacts in either CatWISE or AllWISE, the median (CatWISE - AllWISE) value over the 2.5 to 8 mag range is 0.17 mag in W1 and 0.02 mag in W2, and the median absolute deviation is 0.08 mag in W1 and 0.02 mag in W2). Even though completeness falls rapidly for brighter stars, CatWISE reliability is $\sim 90\%$ or better down to 2.5 mag. For the brightest stars, CatWISE completeness is poor, and CatWISE reliability shows large fluctuations due in part to the resulting small number statistics.

4.1.2. *Faint Sources*

Completeness and reliability were assessed for faint sources using the *Spitzer* South Pole Telescope Deep Field (SSDF) survey (Ashby et al. 2013) as a truth set. The SSDF covers ~ 94 deg^2 with 2 minutes of integration per position with *Spitzer*. *WISE* survey depth increases towards the ecliptic
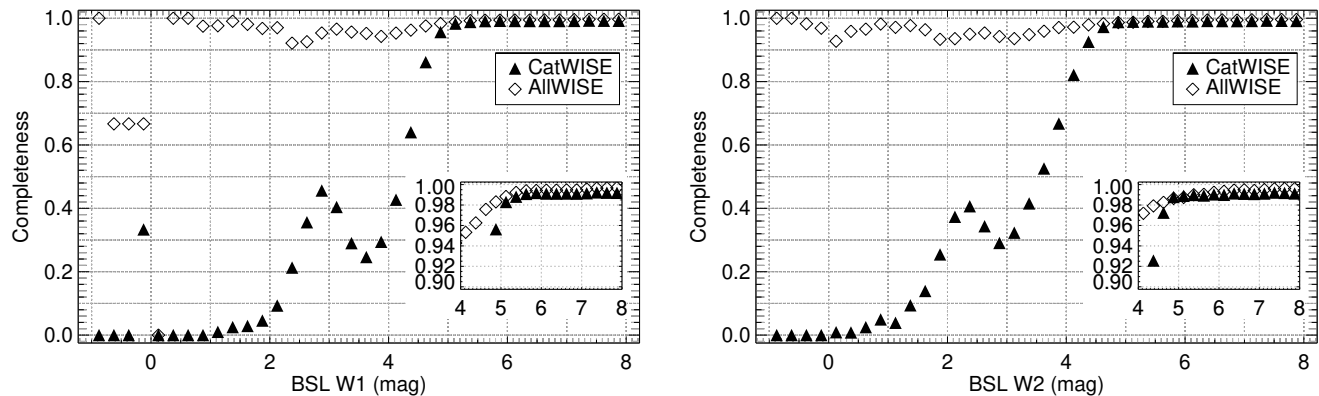
Figure 7. Differential completeness of the CatWISE Preliminary Catalog as a function of the Bright Star List's W1 (left) and W2 (right), compared to AllWISE.
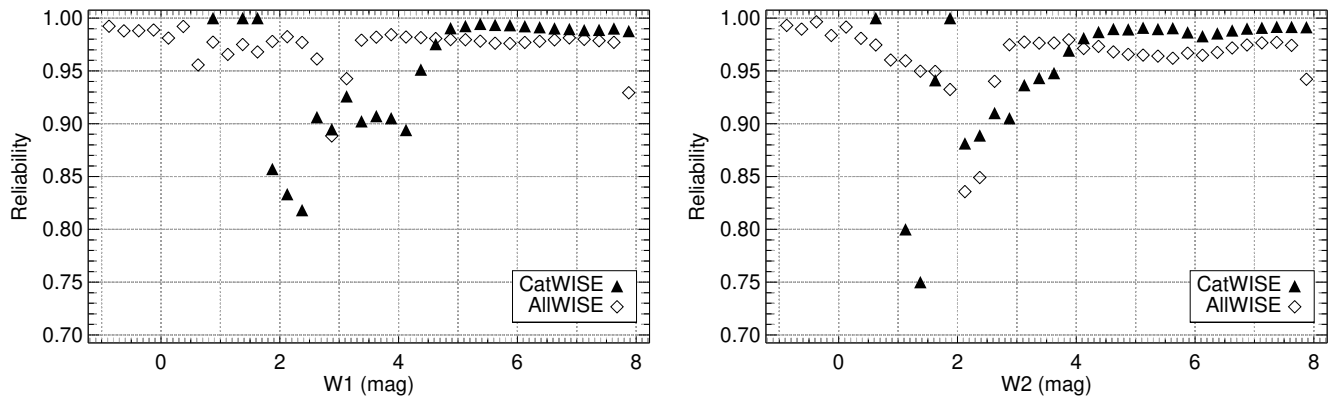

Figure 8. Differential reliability of the CatWISE Preliminary Catalog as a function of the Bright Star List's W1 (left) and W2 (right), compared to AllWISE. Not shown are points at W2=-0.75 mag and +0.75 mag with reliabilities of 0 and 0.5 respectively.

poles, and for the SSDF, with $\beta \sim -46°$, the typical number of CatWISE exposures is 125, or 16 minutes. Nevertheless the larger *Spitzer* mirror diameter (85 cm vs. 40 cm for *WISE*) and better image quality (2" vs. 6") makes the SSDF data more sensitive than CatWISE.

The radius used to match *Spitzer* SSDF sources with CatWISE sources was 2″.5, and otherwise the methodology to determine completeness and reliability was the same as in §4.1.1. The results are shown in Figures 9 and 10.

Figure 9. Completeness of the CatWISE Preliminary Catalog vs. *Spitzer* 3.6μm (left) and 4.5μm (right) magnitude for sources in the SSDF.
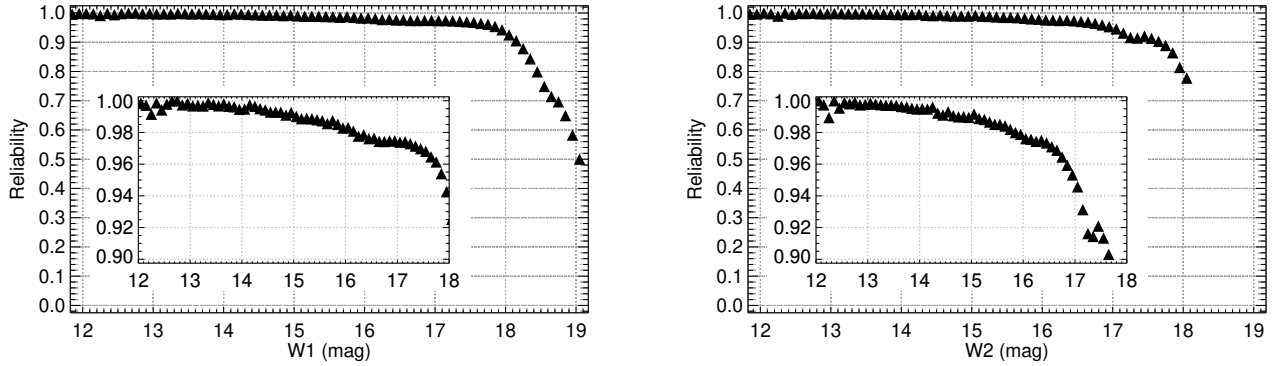

Figure 10. Reliability of the CatWISE Preliminary Catalog as a function of W1 (left) and W2 (right), for sources in the SSDF.

At this coverage depth, the CatWISE Preliminary Catalog completeness is $\sim 98\%$ for sources brighter than 13th mag, consistent with the performance seen from comparisons to the Bright Star List (§4.1.1), and remains above 90% for sources brighter than $[3.6] = 16$ mag or $[4.5] = 15.5$ mag, dropping to 50% at $[3.6] = 17.8$ mag and $[4.5] = 17.4$ mag. The SSDF achieves 55% completeness at $[3.6] = 18.5$ mag and $[4.5] = 18.0$ mag (Ashby et al. 2013).

CatWISE reliability at this coverage depth is better than 99% for sources brighter than 15th mag in both W1 and W2, again consistent with the Bright Star List results. CatWISE reliability remains above 90% to W1 = 18.2 and W2 = 17.6 for this ecliptic latitude and coverage depth. Reliability at fainter magnitudes is not well determined because the SSDF data are not deep enough.

4.2. *Photometric properties*

We assessed CatWISE photometric depth using both the SSDF (§4.1.2) and the COSMOS field. The COSMOS field is an important benchmark for assessing CatWISE performance, because it has been intensively observed, is near the ecliptic ($\beta = -11°$), and is at fairly high Galactic latitude ($b = 41°$). Although confusion effects are reduced by the high Galactic latitude, the ecliptic has the highest zodiacal emission and lowest survey coverage from *WISE*, making COSMOS a representative base for performance estimates.

Figure 11 compares CatWISE Preliminary Catalog PSF-fitting photometry to 2″9 radius aperture photometry from the *Spitzer* S-COSMOS program (Sanders et al. 2007). These observations were obtained using longer integration times (20 minutes) than for the SSDF, while the CatWISE integration is lower (12 minutes) than in the SSDF, so the S-COSMOS data are much deeper than CatWISE. The closest CatWISE source within 2″75 was taken as the match to the S-COSMOS source. Because the CatWISE photometry is point source fitting, S-COSMOS sources were required to have $< 10\%$ flux increase between the 1″9 and 2″9 radius apertures. In addition, because the W1 band is significantly bluer than the [3.6] band, S-COSMOS sources at [3.6] were required to have $-0.1 \leq [3.6] - [4.5] \leq 0$ (see Figures 2 and 3 in §VI.3.a of the All-Sky Explanatory Supplement; Cutri et al. 2012). While necessary for comparing W1 and [3.6] photometry, the color cut significantly reduces the numbers of sources for comparison. Figure 12 gives the analogous comparison to photometry from the SSDF survey.

The comparison between the CatWISE and *Spitzer* photometry is consistent for both fields, in both bands. CatWISE photometry becomes ~ 0.1 mag fainter than *Spitzer* beyond 16th mag, possibly due to the increasing incidence of extragalactic sources at faint magnitudes. The measured scatter in the SSDF reaches 0.217 mag, equivalent to an SNR of 5, at $[3.6] = 17.64$ mag and $[4.5] = 16.49$ mag. Adjusting for the mean offsets in W1–[3.6] and W2–[4.5] at these magnitudes, and subtracting 0.14 mag to adjust the SSDF 125 exposure depth to the 96 exposure depth that we take as the baseline for the CatWISE Preliminary Catalog, we find that the SNR=5 limits for CatWISE are W1=17.67 mag and W2=16.47 mag.
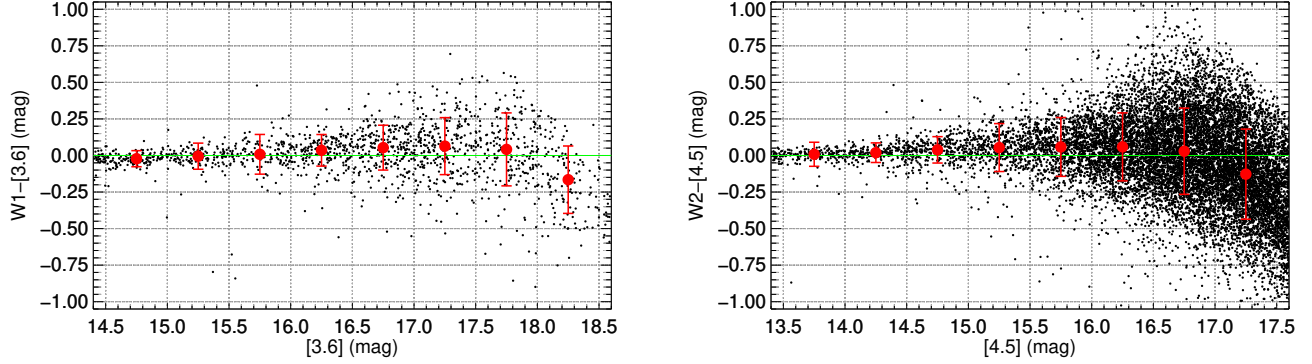
Figure 11. Comparison of CatWISE photometry to *Spitzer* photometry for COSMOS. *Left*: Difference between CatWISE W1 PSF and *Spitzer* S-COSMOS $2\rlap{.}{''}9$ radius aperture photometry at [3.6], for sources with $-0.1 < [3.6] - [4.5] < 0$ and $< 10\%$ flux increase from the $1\rlap{.}{''}9$ to $2\rlap{.}{''}9$ aperture. Median differences and standard deviations in 0.5 mag bins are shown by the red points and error bars. *Right*: The analogous comparison for CatWISE W2 and *Spitzer* [4.5] photometry, but without the restriction on *Spitzer* source color.

Figure 12. Comparison of CatWISE photometry to *Spitzer* photometry for the SSDF, using the same methodology as in Figure 11. The outer contour represents a source density of 10 sources per 0.05×0.05 mag bin, with each additional contour showing a factor of two increase in source density. Note the three additional contour levels on the right, due to the lack of the color cut used on the left.

4.3. *Astrometric properties*

4.3.1. *Full-sky Astrometric Assessments*

The astrometric performance of CatWISE was assessed by comparing to *Gaia* DR2 (Gaia Collaboration et al. 2018; Lindegren et al. 2018). Within each tile, the 10 brightest sources in bins of 0.5 mag over the $10 <$W1< 17.5 mag range were selected, providing a sample of 150 sources per tile, uniformly

distributed on the sky. At low Galactic latitudes, CatWISE does not reach to W1=17.5 mag, and therefore the faintest bins are empty. The sample for astrometric comparison consists of 2,699,315 sources. These sources were cross-matched with *Gaia* DR2 using a 5″.5 radius (corresponding to two *WISE* pixels), requiring the *Gaia* counterpart to have measured proper motions. This returned 2,148,274 unique matches. The completeness of the match approaches 100% for sources brighter than W1=14 mag, and drops to ∼ 25% at the faintest magnitudes. *Gaia* astrometry was used to propagate the *Gaia* counterparts to the CatWISE epoch, and the standard deviation[4] between the CatWISE motion-fit and *Gaia* position and motion values was computed.

Figure 13 summarizes the results of the full sky comparison. The positional accuracy floor for bright sources approaches ∼ 50 mas and remains approximately constant until W1∼ 12.5 mag. At fainter magnitudes, the dispersion increases to 275 mas (1/10 of a pixel) at W1∼ 15.5 mag, while in the faintest magnitude bin the dispersion is ∼ 700 mas, with the dispersion in α being slightly better than in δ. This is expected since the scan direction is closer to δ and the PSF is more elongated in the scan direction. At the bright end, however, the accuracy in δ is better than in α, an effect not fully understood.

The motion accuracy floor for bright stars is just under $10 \, \mathrm{mas \, yr^{-1}}$, consistent with the positional accuracy floor – given CatWISE's 6 year baseline, and since the motion accuracy scales linearly with time, one would expect $\sigma_\mu \sim \sigma_{\mathrm{pos}}/6$. At W1∼15.5 mag, the motion accuracy is $\sim 30 \, \mathrm{mas \, yr^{-1}}$, a factor of 10 better than AllWISE (Kirkpatrick et al. 2014). At the faint end, CatWISE is sensitive to proper motion of $100 \, \mathrm{mas \, yr^{-1}}$ until W1∼17 mag.

The two panels on the right of Figure 13 show the χ^2 computed using the CatWISE catalog uncertainties, the *Gaia* catalog uncertainties, and the uncertainty introduced by the translation of the *Gaia* position to the CatWISE epoch. Since the total uncertainty is dominated by CatWISE, these χ^2 values are essentially a measurement of how accurate the CatWISE Preliminary Catalog uncertainties are. The expected value of the median χ^2 with one degree of freedom is ∼ 0.45, so

---

[4] The IDL "robust_sigma" function was used to calculate the standard deviation.
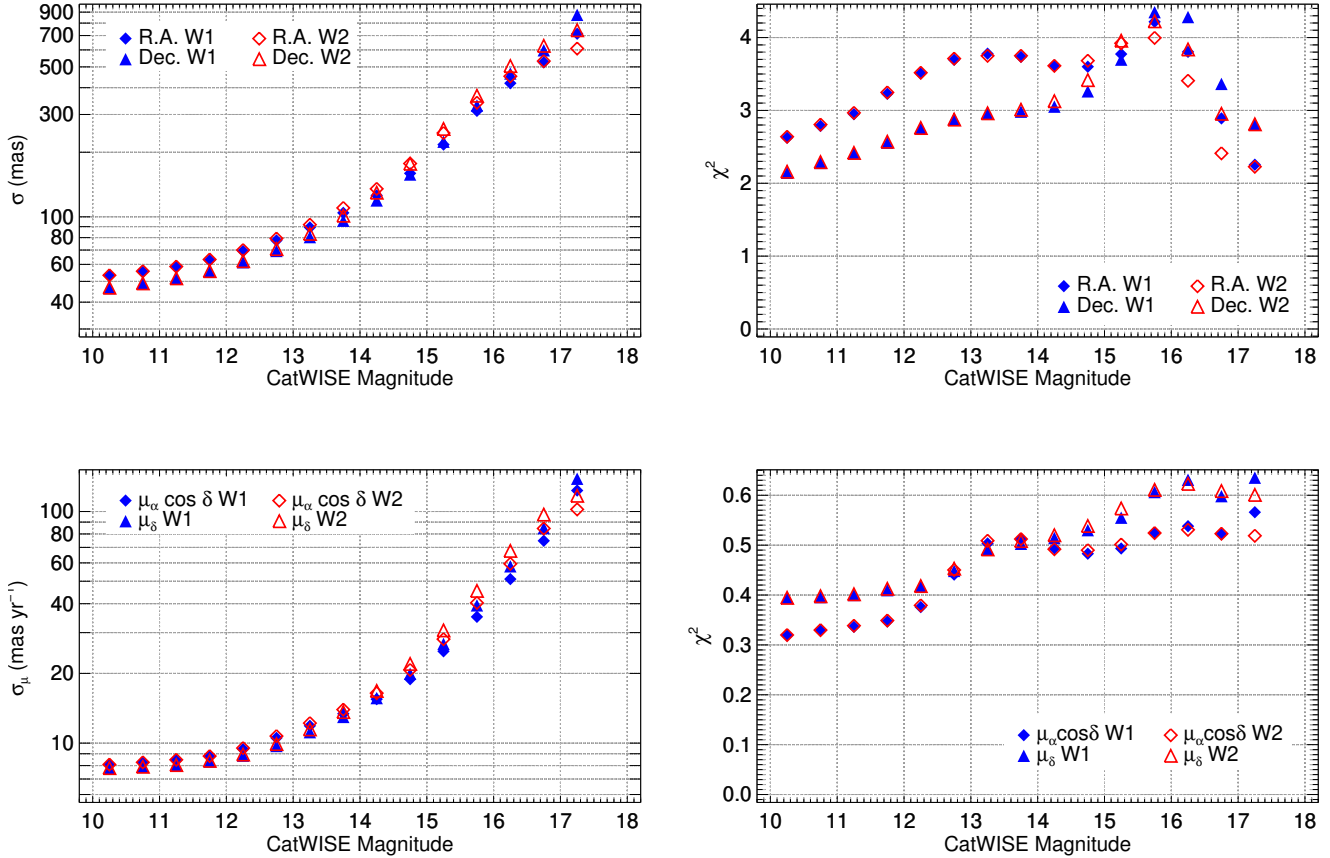
Figure 13. CatWISE astrometric performace with respect to *Gaia* DR2. *Left:* the 1-σ dispersion between CatWISE and *Gaia* R.A. (specifically, $\Delta\alpha \cos(\delta)$) and Dec. (top) and proper motion (bottom), for a subsample of $\sim$2.1 million sources in the $10 <$W1< 17.5 mag range, uniformly distributed over the entire sky. *Right:* the median χ^2 computed taking into account CatWISE catalog uncertainties, *Gaia* catalog uncertainties, and the uncertainty introduced by the translation of *Gaia*'s positions to the CatWISE epoch.

the top right panel of Figure 13 indicates that the catalog position uncertainties underestimate the actual errors by a factor of 2.5–3. In contrast, the motion uncertainties are consistent with the expected value. We have not investigated the reason for this, although it suggests an additional error in position that is stable for a given source. Confusion is one possible explanation. Although the uncertainties are underestimated, the actual CatWISE position errors are comparable to those for AllWISE (see §II.5.c of the AllWISE Explanatory Supplement (Cutri et al. 2013).
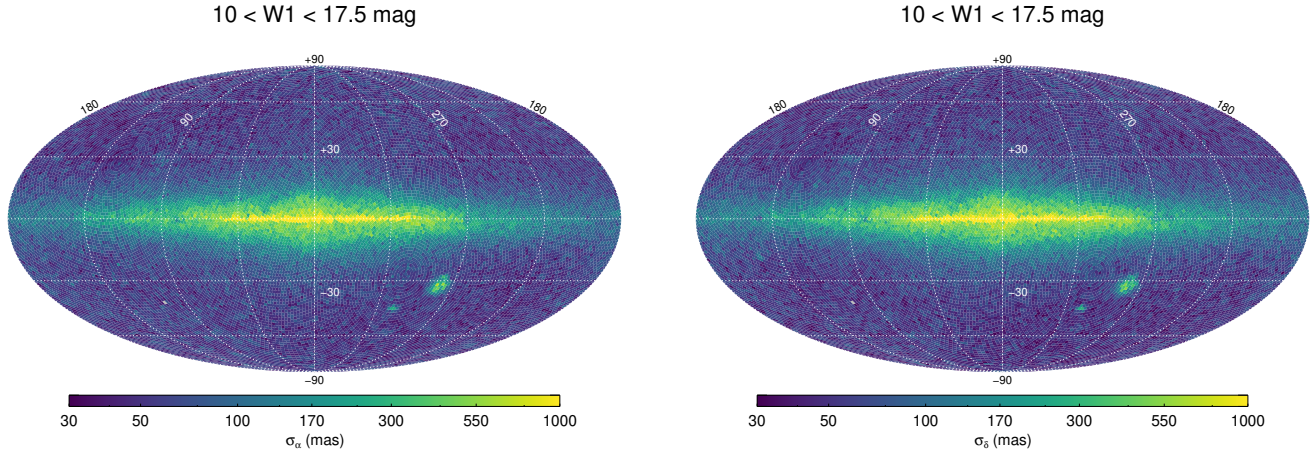
Figure 14. 1-σ dispersion of the CatWISE α (left) and δ (right) with respect to *Gaia* DR2, for sources in the $10 <$W1< 17.5 mag range.

The astrometric performance is however not uniform over the sky. Figures 14–17 show the 1-σ dispersion in each tile with respect to *Gaia* positions and motion components for the full magnitude range considered (Figures 14 and 16), and in three smaller magnitude intervals (Figures 15 and 17). The maps for the full magnitude range are smooth overall, indicating a fairly constant astrometric performance for CatWISE over the majority of the sky. The main features can be easily identified – the Galactic plane (and in particular the bulge), and the Small and Large Magellanic Clouds (SMC and LMC). In those denser regions, the astrometric accuracy for the bright stars deteriorates to ~ 500 mas for positions and ~ 30 mas yr^{-1} for motions, and to $\sim 1,000$ mas and ~ 200 mas yr^{-1} (or worse) for the faint stars.

The motion accuracy maps show additional features that appear to be related to the *WISE* survey strategy, and to the transition between the cryogenic and post-cryogenic phases of the mission. In particular, one can see better motion performance approaching the ecliptic poles (at $l = 96°; b = 30°$ and $l = 276°; b = -30°$, respectively) compared to regions of similar Galactic latitude. This is a result of the increased coverage of the sky by *WISE* at higher ecliptic latitude. Conversely, there are two strips of slightly poorer motion performance, which are coincident with the transition between
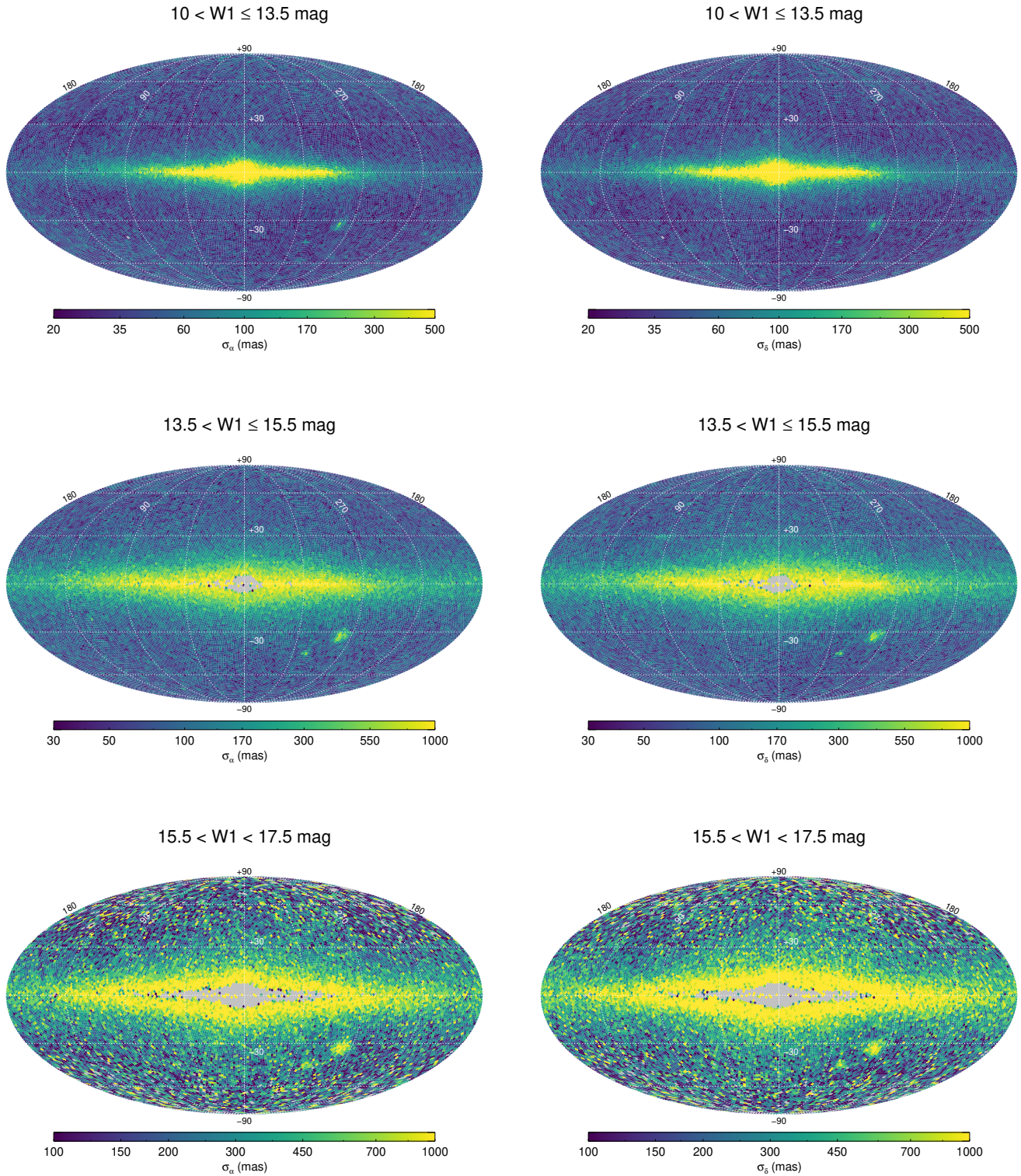
Figure 15. Same as Figure 14, but for three W1 magnitude ranges. Gray tiles are those where there were no sources in CatWISE in the given magnitude bin.
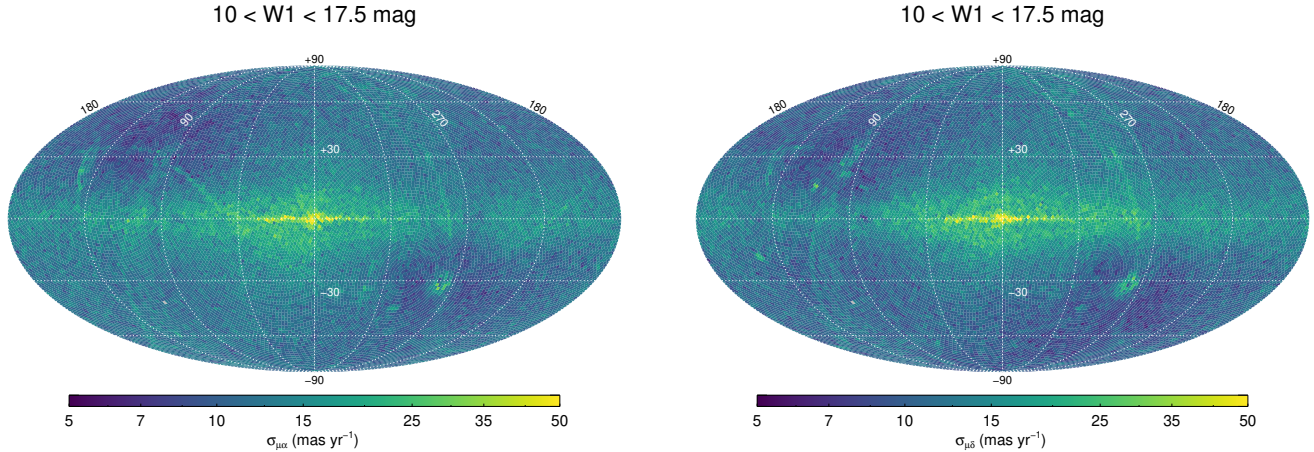
Figure 16. Same as Figure 14, but for the proper motion components.

cryogenic and post-cryogenic phases, where the PSF was changing rapidly as the telescope was warming up.

The maps for the faintest magnitude interval appear noisy. This is partly intrinsic, and partly an effect of statistical fluctuations due to the low number of sources with a *Gaia* counterpart in each tile (as discussed above, the completeness for the *Gaia* match drops to $\sim 25\%$ at the faint end). Moreover, at lower Galactic latitudes, CatWISE detects only brighter sources because of confusion noise.

4.3.2. *Astrometric Assessments in Selected Tiles*

We next consider the astrometric performance in more detail by focusing on four tiles:

- the North Ecliptic Pole tile (NEP, tile 2709p666), a field with maximal *WISE* coverage and average source density;

- the South Ecliptic Pole tile (SEP, tile 0890m667) a field with with maximal *WISE* coverage and high source density (the SEP tile contains part of the LMC);

- the Galactic Center tile (GC, tile 2657m288) a field with average *WISE* coverage and maximal source density; and
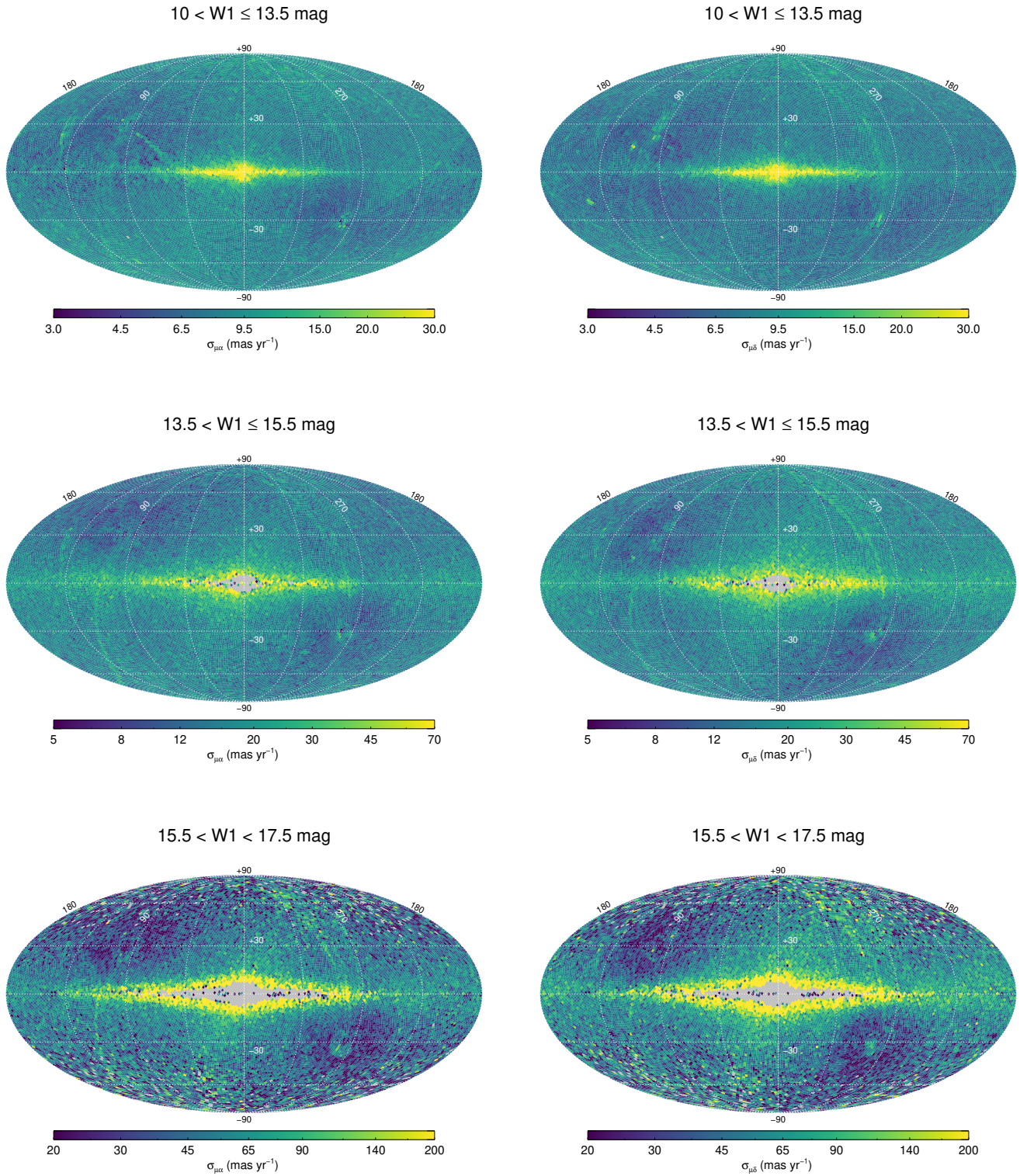
Figure 17. Same as Figure 16, but for three W1 magnitude ranges. Gray tiles are those where there were no sources in CatWISE in the given magnitude bin.

- the COSMOS tile (tile ID 1497p015), representative of most of the sky, i.e. a field with average *WISE* coverage and source density.

The analysis of §4.3.1 was repeated for these four tiles, but using all of the sources in each tile. The results are shown in Figure 18 and 19. We then defined ten metrics to characterize the astrometric performance of CatWISE:

- $\sigma_{\min}$ and $\sigma_{\mu,\min}$ are the accuracy floor for positions and motions, respectively. These accuracy floors are determined as the median dispersion with respect to *Gaia* in the $8 < \text{W1,W2} < 10$ mag interval, except in the GC where we restrict to $8 < \text{W1,W2} < 9$ mag since the astrometric accuracy starts deteriorating significantly beyond W1,W2~9 mag (see Figure 18–19).

- $\text{W1}_{\min}$, $\text{W2}_{\min}$, $\text{W1}_{\mu,\min}$, and $\text{W2}_{\mu,\min}$ are the W1 and W2 mag at which $\sigma_{\min}$ and $\sigma_{\mu,\min}$ are exceeded by no more than 20 mas and 5 mas yr^{-1}, respectively.

- W1_{500} and W2_{500} are the W1 and W2 mag at which the accuracy on positions reaches 500 mas.

- $\text{W1}_{\mu,100}$ and $\text{W2}_{\mu,100}$ are the W1 and W2 mag at which the accuracy on motion reaches 100 mas yr^{-1}.

The results for the four representative tiles are summarized in Table 3.

For brighter sources, $\sigma_{\min}$ and $\sigma_{\mu\min}$ are encouragingly small, on the order of 40 mas and 8 mas yr^{-1}, respectively. $\text{W1}_{\min}$ and $\text{W2}_{\min}$ are ~ 12 mag while $\text{W1}_{\mu,\min}$ and $\text{W2}_{\mu,\min}$ are ~ 14.5 mag. All the above metrics show little dependence on coverage and source density, except for the GC tile, where they are degraded to $\sigma_{\min} \sim 530$ mas, $\sigma_{\mu,\min} \sim 20$ mas, at a limiting depth of only ~ 8 mag and ~ 9 mag respectively. This is consistent with the uniformity of the maps in Figures 14 to 17.

For fainter sources, W1_{500}, W2_{500}, $\text{W1}_{\mu,100}$ and $\text{W2}_{\mu,100}$ show a clearer dependence on source density and coverage. For COSMOS (i.e. a typical CatWISE tile) these metrics are ~ 17 mag. W1_{500} and W2_{500} become ~ 9 mag shallower in the GC, while $\text{W1}_{\mu,100}$ and $\text{W2}_{\mu,100}$ measurements are upper limits only. This is again a consequence of the fact that at lower Galactic latitudes CatWISE only detects brighter sources because of confusion noise, and for sources this bright the motion accuracy never degrades to the 100 mas yr^{-1} level.

Table 3. CatWISE Astrometric Performance Evaluation Fields

	0890m667	1497p015	2657m288	2709p666
	SEP, LMC	COSMOS	GC	NEP
l (deg)	276.5	237.3	359.8	96.4
b (deg)	-30.2	41.4	0.6	29.5
β (deg)	-89.6	-10.2	-5.4	89.6
Exp.	7154	90	86	7839
#	71462	58961	63368	61702
$\sigma_{\min}$ (mas)	52.9	27.3	526.4	37.7
$W1_{\min}$ (mas)	11.0	12.5	8.0	12.0
$W1_{500}$ (mag)	15.1	17.0	8.4	18.5
$W2_{\min}$ (mag)	11.0	12.5	8.0	12.0
$W2_{500}$ (mag)	15.0	16.8	8.3	19.0
$\sigma_{\mu,\min}$ (mas yr^{-1})	7.4	8.5	22.2	7.3
$W1_{\mu,\min}$ (mag)	14.5	13.5	9.0	15.5
$W1_{\mu,100}$ (mag)	18.2	16.8	> 11.0	> 19.0
$W2_{\mu,\min}$ (mag)	14.5	13.5	9.0	15.5
$W2_{\mu,100}$ (mag)	>20.5	16.7	>11.5	>20.0

NOTE— l, b, and β are the Galactic longitude, Galactic latitude, and ecliptic latitude for the center of the tile, in degrees. Exp. indicates the number of exposures for the tile, # the number of sources (combining catalog and reject entries). The subsequent metrics are described in detail in §4.3.

$W1_{\mu,100}$ and $W2_{\mu,100}$ become ~2 mag deeper (~19 mag) at the ecliptic poles, thanks to the higher coverage. $W1_{500}$ and $W2_{500}$ are much deeper at the NEP than the SEP, most likely an effect of the much higher source density at the SEP, and therefore the higher confusion noise. However, this does not seem to affect the motion metrics.
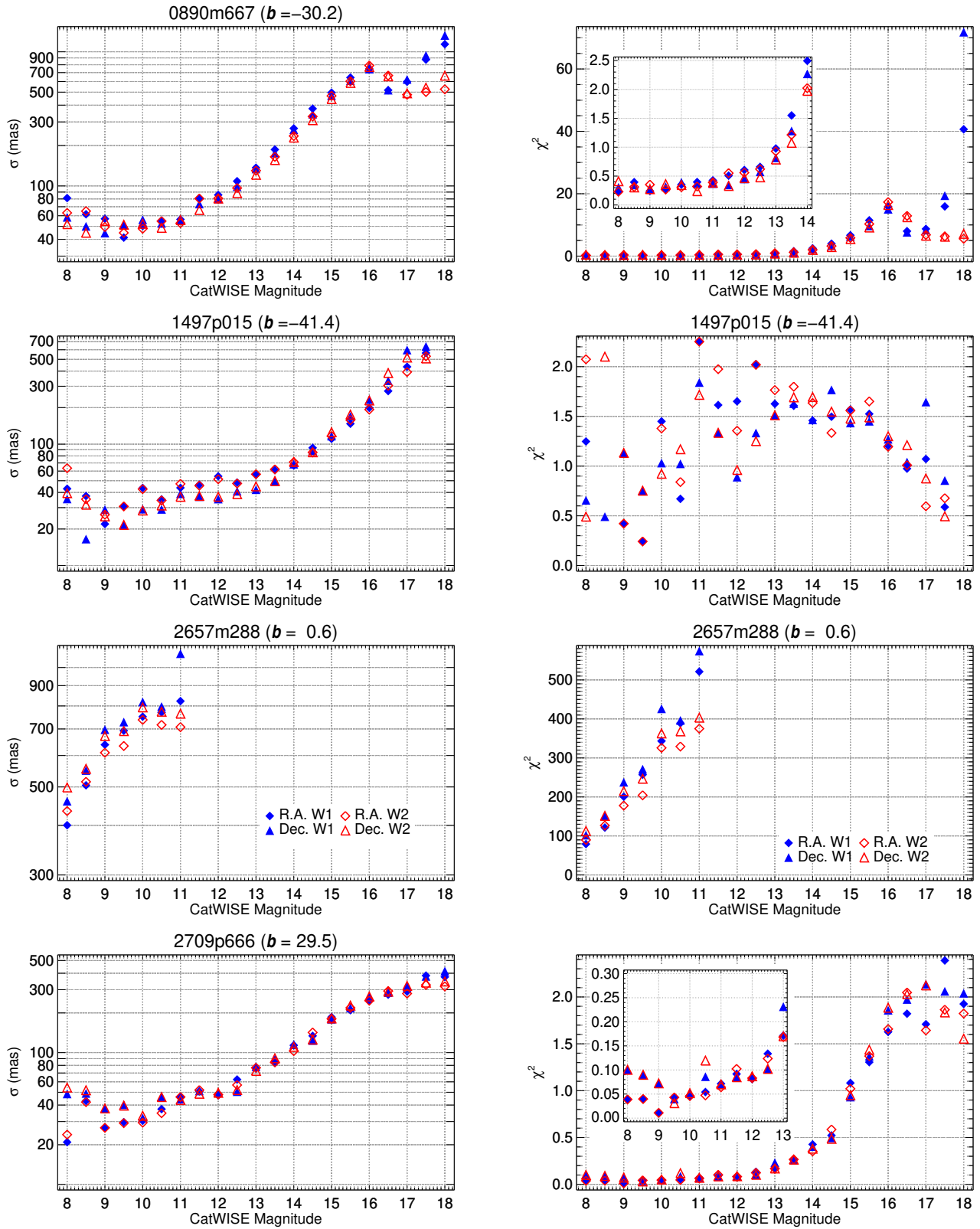
Figure 18. Same as Figure 13, but for four tiles: the SEP (0890m667), COSMOS (1497p015), the GC (2657m288), and the NEP (2709p666). The standard deviation between CatWISE position measurements and *Gaia* DR2 position measurements, and the corresponding χ^2 in 0.5 mag bins, is shown in red (R.A.) and blue (Dec.).
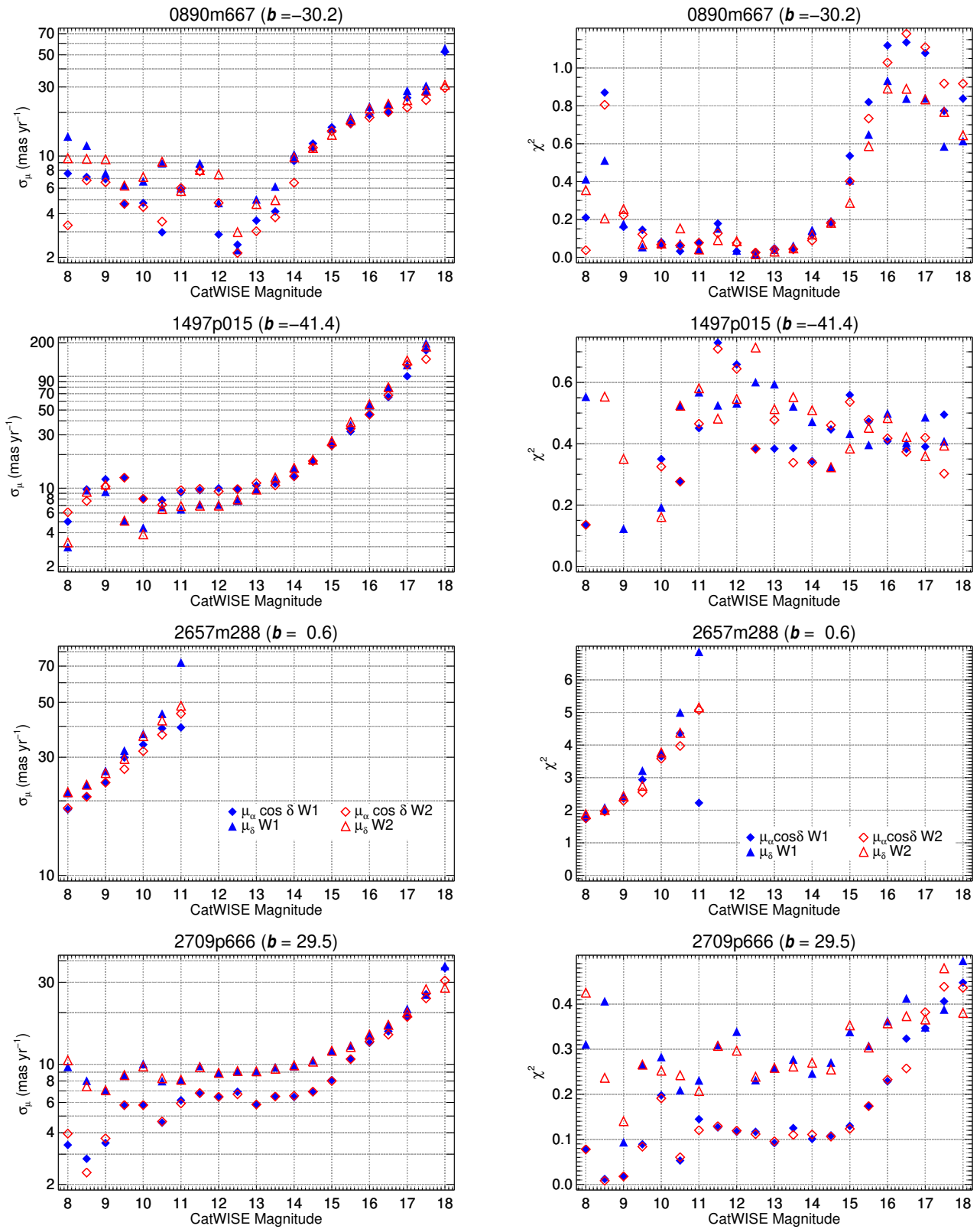
Figure 19. Same as Figure 18, but for motion measurements.

4.3.3. *Fast Movers*

We compared the astrometric performance using merged results from ascending and descending scans processed with separate PSF's to that using a single PSF per band for all scans processed together (see §3.4) on a set of 19 known ultracool dwarfs, chosen from the literature. Our test set included extremely cold, very fast moving objects (e.g. WISE J085510.83–071442.5, $\mu_{\rm tot} \sim 8$ arcsec yr^{-1}; Luhman 2014), as well as warmer, slower M dwarfs (e.g. WISE J072003.20–084651.2, $\mu_{\rm tot} \sim 0.12$ arcsec yr^{-1}; Scholz 2014). Results using separate PSF's proved superior, delivering good motion measurements for 17 out of the 19 test objects, while the single PSF option only recovered 13 out of the 19 test objects, with a clear drop in performance for objects with $\mu_{\rm tot} \gtrsim 2.5$ arcsec yr^{-1}. Only one out of the five fastest moving objects in our test sample is correctly measured using the single PSF method, while using separate ascending and descending scan PSF's and merging the results measures four out of these five.

The two objects that our pipeline is unable to correctly measure – WISE J163940.83–684738.6 and WISEPC J205628.90+145953.3 – are missed at the detection stage (§3.3) because they are partly blended with brighter nearby sources. These two sources were recovered when the detection step was run without the PSF convolution (§3.1 and 3.3), yielding reasonable motions, but they are not present in the CatWISE Preliminary Catalog.

The fastest movers in our test set have larger parallaxes (up to 502 mas for WISE J104915.57-531906.1, Lazorenko & Sahlmann 2018), which will affect motion measurements when measuring ascending and descending scans together. To test this, we also processed the fastest movers using a single PSF but measuring ascending and descending scans separately and merging them. This gave better performance than processing scans together, recovering motions correctly for three of the five fastest movers.

Comparing astrometry to *Gaia* for all sources in these tiles showed that even when measuring ascending and descending scans separately and merging them, using separate PSFs further improves performance. The position sigmas were 10% to 20% better at all magnitudes when using separate PSFs than when using a single PSF. For brighter sources (< 12 mag), motion sigmas improved by

$\sim 20\%$ using separate PSFs, while at fainter magnitudes the single and separate PSFs yielded similar motion sigmas. Processing ascending and descending scans separately was beneficial both because it allowed the PSF asymmetry to be addressed, and because it removed the effect of parallax on measured motions.

5. EXAMPLE SCIENCE APPLICATIONS

An initial application of the CatWISE catalog was the first secure W2 detection for the Y dwarf WD0806-661 B (Meisner et al. 2018b), leading to a [4.5] - W2 color consistent with the population of known Y dwarfs. CatWISE represents a major hunting ground for cold brown dwarfs. The improved depth (§4.2) and motion sensitivity (§4.3) allows for a deeper, more complete search for the coldest constituents of the solar neighborhood, a crucial population if we wish to constrain the low-mass end of the mass function (see e.g. Kirkpatrick et al. 2019).

Towards this goal we are mining CatWISE using both a "classical" and a "machine learning based" approach. Here "classical" means a search based on color and motion cuts applied to the catalog data to select cold brown dwarf candidates, while machine learning uses the previously known population of cold brown dwarfs as a training set to develop a classifier that is then applied to the CatWISE catalog.

Early results include the discoveries of CWISEP J193518.59–154620.3 (Marocco et al. 2019) and WISEP J144606.62–231717.8 (Marocco et al. 2020), two of the coldest brown dwarfs identified to date, with infrared colors comparable with those of the coldest brown dwarf known, WISE J085510.83–071442.5 (Luhman 2014). *Spitzer* follow-up of additional cold brown dwarf candidates is presented in Meisner et al. (2019b).

Prospects are also good for discovering distant galaxy clusters using CatWISE. Gonzalez et al. (2019) used the AllWISE Catalog together with Pan-STARRS to carry out the Massive and Distant Clusters of WISE Survey (MaDCoWS), identifying over 2000 galaxy cluster candidates with photometric redshifts in the $0.7 - 1.5$ range. The additional depth of CatWISE compared to AllWISE increases the W1 detection limit for L* galaxies from $z \sim 0.8$ to $z \sim 2$. Figure 20 illustrates the increase in the number of distant galaxies with substantial photometric redshifts in the COSMOS
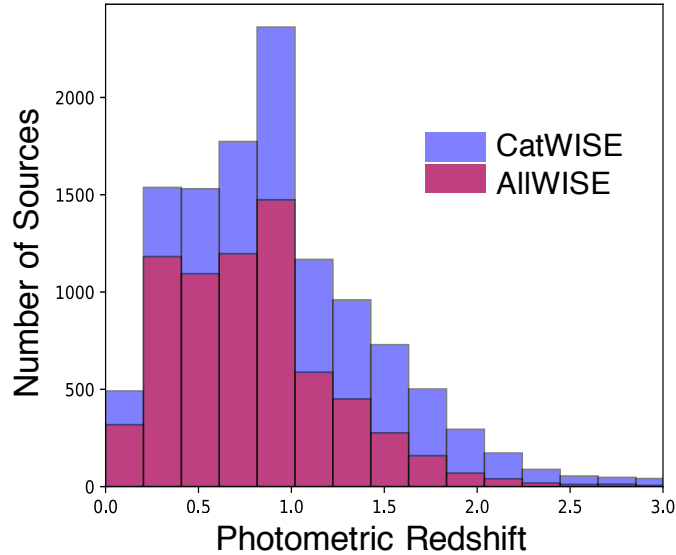
Figure 20. CatWISE detects sources ~ 0.5 mag fainter than AllWISE, providing many times more sources at $z > 1.5$. The vertical axis is the number of COSMOS sources that were detected by CatWISE and AllWISE in the 1497p015 tile and had matches within $2.''5$ of sources with the indicated photometric redshifts from Laigle et al. (2016).

field (Laigle et al. 2016) detected by CatWISE compared to AllWISE. Between $z = 1.5$ and 1 clusters transition from being more actively star-forming than the field to being mainly quiescent in terms of star formation (e.g., Brodwin et al. 2013), so CatWISE offers the potential of reaching the era where major formation and assembly of clusters is underway.

Finally, the AllWISE Catalog played an important role in the discovery of ULAS J1342+0928, at $z = 7.54$ the most distant quasar known (Bañados et al. 2018). The additional depth of CatWISE may enable extending this to redshifts as large as 9, when the seeds of reionization were emerging in the overwhelmingly neutral Universe. With over 3000 refereed papers making use of the existing *WISE* catalogs, many other uses for CatWISE can be anticipated.

6. DATA ACCESS

Current information about CatWISE data products is provided at https://catwise.github.io.

The merged Preliminary catalog and reject files are available from IRSA (https://irsa.ipac.caltech.edu) in the WISE/NEOWISE Enhanced and Contributed Products area. IRSA's catalog search tools

allow for complex search queries. IRSA also hosts the AllWISE Explanatory Supplement (Cutri et al. 2013), which provides full details on the AllWISE processing algorithms, and includes descriptions of the AllWISE Catalog columns, many of which are applicable to CatWISE. Appendix A provides additional information about CatWISE columns.

The individual tile files have also been transferred to a data repository at the National Energy Research Scientific Computing Center (NERSC), and are available at https://portal.nersc.gov/project/cosmo/data/CatWISE/prelim in 18,240 pairs of gzipped ASCII files (one catalog and one reject file per tile) in IPAC table format, organized into 359 directories, one for each decimal degree of right ascension from 0° to 358° (there are no tiles beginning with 359). Text files providing the format and a brief description of the columns in the catalog and reject files are also provided there. The catalog and reject files for the 50 tiles near the ecliptic poles (Table 1), where a single PSF per band was used for processing, include the string "opt0" in their names. Files for tiles where different PSFs were used for ascending and descending scans (§3.2) include the string "opt1" in their names.

ACKNOWLEDGMENTS

APPENDIX

A. CATWISE PRELIMINARY CATALOG COLUMN DESCRIPTIONS

We adopt MJD 56700 (2014 Feb. 12) as the epoch for reporting positions when solving for source motion in the Preliminary Catalog. Source positions, whether incorporating source motion or not, are given in the equinox J2000 coordinate frame. Column entries involving right ascension that are in units of arcseconds have the cos(declination) term applied. The convention for designating sources from the CatWISE Preliminary Catalog and Reject Table is specified in §3.7.

There are 186 formatted columns of information about each source in the CatWISE Preliminary Catalog. The CatWISE Preliminary Reject Table adds a column to indicate whether the source is "primary" (see §3.6). Descriptions of nearly all the columns can be obtained from IRSA at https://irsa.ipac.caltech.edu/data/WISE/CatWISE/gator_docs/catwise_colDescriptions.html. Most of the columns have the same names as in the AllWISE Catalog, and are described in §II.1.a of the AllWISE Explanatory Supplement (Cutri et al. 2013). Table 4 provides information about selected columns in the CatWISE Preliminary Catalog that augments or supersedes the information provided by IRSA. Four columns (*w1fitr, w2fitr, glon, glat*) in the NERSC release are hidden in the IRSA release, and their names are shown in parentheses in Table 4.

Table 4. Additional Information on CatWISE Preliminary Catalog Columns

Name	Units	Type	Format	Description
(w1fitr)	arcsec	R*4	f7.2	Fitting radius for W1. In the CatWISE Preliminary Catalog, w1fitr and w2fitr are always -99.99, 7.5, or 13.2. Both are hidden in the IRSA release, because they do not appear to follow the prescription given in http://wise2.ipac.caltech.edu/docs/release/allsky/expsup/sec4_4c.html#wpro where rfit=1.25 FWHM (7″.5 for W1 and W2) or $2r_{sat}$ (saturation radius), whichever is larger.
(w2fitr)	arcsec	R*4	f7.2	Fitting radius for W2. See w1fitr.
dist_ad	arcsec	R*4	f9.3	Radial distance between ascending and descending apparitions. The field name in the IRSA release is dist_ad, but in the NERSC release, this field is called dist.
elon_avg	deg	R*8	f11.6	Averaged ecliptic longitude between ascending and descending apparitions
elat_avg	deg	R*8	f11.6	Averaged ecliptic latitude between ascending and descending apparitions
chi2pmra	...	R*4	1pE10.3	χ^2 for difference between PMRA for ascending and descending apparitions (1 degree of freedom)
chi2pmdec	...	R*4	1pE10.3	χ^2 for difference between PMDec for ascending and descending apparitions (1 degree of freedom)
par_pm	arcsec	R*4	f11.3	Parallax estimate from motion solution. Computed using PMRA and PMDec to propagate ascending and descending motion solution positions to MJD 56700, then dividing ecliptic longitude difference by 2. Because scan longitudes on opposite sides of orbit had a 5° bias from a great circle until the end of 2014, gradually increasing to 18° by the end of 2017, the actual baseline is < 2au, declining from 1.996 to 1.951 au over this period, although the difference is negligible given the uncertainty in parallax. Will be null unless km = 3.

Table 4 *continued on next page*

Table 4 *(continued)*

Name	Units	Type	Format	Description
par_stat	arcsec	R*4	f11.3	Parallax estimate from stationary solution. Computed using PMRA and PMDec to propagate ascending stationary-solution position from ascending observation epoch to descending observation epoch, then dividing ecliptic longitude difference by 2 (see entry for par-pm regarding dividing by 2). Will be null unless ka = 3, km > 0, and all w?mjdmin/max/mean values are non-null in both ascending and descending WPHOT output.
dist_cc	arcsec	R*4	f13.3	Maximum distance between CatWISE and AllWISE sources providing cc_flags. See §3.5.1. In the NERSC release, this field is called dist_x.
cc_flags	⋯	char	a16	Worst case character cc_flag from AllWISE. See §3.5.1.
w1cc_map	⋯	int	i13	The description in the AllWISE Explanatory Supplement is incorrect, so an updated description is provided here. Worst case contamination and confusion map in W1 for matching AllWISE sources. Contains integer equivalent of 12-bit binary number specifying if W1 measurement in AllWISE is believed to be contaminated by or a spurious detection of an image artifact. Elements of binary array (with bit number indicated below each code) are given in Table 5. Bits 0, 1, 3 and 4 indicate whether band-detection is contaminated by an artifact. If brightness of detection is less than expected for artifact, source is regarded as spurious and bits 7, 8, 10, and 11 are also set accordingly. Letters denote contamination by different types of artifacts (see §3.5). For example, a measurement believed to be a spurious detection of a scattered light halo and contaminated by a diffraction spike has a binary bit map value of "010000001001" and w1cc_map=1033. When there is more than one AllWISE match to a CatWISE source, a logical 'OR' is performed over all the matches for each bit.

Table 4 *continued on next page*

Table 4 (*continued*)

Name	Units	Type	Format	Description
w1cc_map_str	⋯	char	a20	The w1cc_map_str description in the AllWISE Explanatory Supplement is incorrect, so an updated description is provided here. Worst case contamination and confusion string in W1 for matching AllWISE sources. This character string denotes all artifacts that may contaminate the AllWISE W1 measurement of this source, in the priority order D,d,P,p,H,h,O,o. For example, a real detection contaminated by a diffraction spike and a latent (persistent) image has a w1cc_map_str="dp". A spurious detection of a diffraction spike also contaminated by a latent image has w1cc_map_str="Dp". This string is "null" if there are no artifacts that affect the measurement in this band. The value that appears in first element of the cc_flags string is the left-most character in w1cc_map_str. If w1cc_map_str is "null", then the corresponding cc_flags entry is "0".
w2cc_map	⋯	int	i13	Worst case w2cc_map from AllWISE. See w1cc_map.
w2cc_map_str	⋯	char	a20	Worst case w2cc_map_str from AllWISE. See w1cc_map_str.
ab_flags	⋯	char	a9	Two character (W1 W2) artifact flag. See §3.5.2.
w1ab_map	⋯	int	i9	W1 artifact code value. See §3.5.2.
w1ab_map_str	⋯	char	a13	W1 artifact string. See §3.5.2.
w2ab_map	⋯	int	i9	W2 artifact code value. See §3.5.2.
w2ab_map_str	⋯	char	a13	W2 artifact string. See §3.5.2.
(glon)	deg	R*8	f12.6	Galactic longitude, calculated using a pole of $\alpha = 192.85°$ $\delta = 27.13°$, and a zero of longitude of $\alpha = 266.4°$ $\delta = -28.94°$ (both in J2000). Hidden in IRSA. See Appendix B for details.
(glat)	deg	R*8	f12.6	Galactic latitude. Hidden in IRSA. See glon.
p	⋯	int	i6	Flag to indicate if source is "primary" in tile. See §3.6.

Table 5. cc_map Bit Definitions

O	H	0	P	D	0	0	o	h	0	p	d
11	10	9	8	7	6	5	4	3	2	1	0

B. CAVEATS

The CatWISE Preliminary Catalog contains a number of features that users should be aware of. Among these are:

- The number of sources per square degree has relatively small variation over the sky (Figure 5).

- Catalog performance is less good in high source density regions (the Galactic plane and the ecliptic poles). Figures 14 through 19 and Table 3 illustrate this.

These issues appears to arise in the detection step. Relatively few deblended sources are added in the measurement step. We are using the unWISE Catalog (which contains many more sources in high density regions; Schlafly et al. 2019) as a detection list for an updated version of the CatWISE catalog that is expected to be available in 2020.

- The completeness and reliability for bright sources is low (Figure 7).

As an example, the brightest two catalog sources in W2 (CWISEP J005153.01–235140.3 and CWISEP J223327.80+060246.2) are spurious, and it is likely that other spurious bright sources are present in the catalog. Users should visually inspect interesting sources selected from the catalog using AllWISE or unWISE images before devoting significant resources to follow up observations.

Additional features present in the CatWISE Preliminary Catalog include:

- Tabulated position uncertainties are significantly smaller than measured position scatter with respect to *Gaia*, as illustrated in Figure 13 (upper right) and Figure 18 (right).

- A floor of 10 mas yr^{-1} was imposed on the tabulated motion uncertainties, making them significantly larger than the measured scatter with respect to *Gaia* motion, as illustrated in Figure 13 (lower right) and Figure 19 (right).

- The Galactic coordinates in the CatWISE Preliminary Catalog were calculated using a pole of $\alpha = 192.85°$ $\delta = 27.13°$, and a zero of longitude of $\alpha = 266.4°$ $\delta = -28.94°$ (both in J2000). These directions are not perpendicular by $22\rlap{.}''663$, and consequently yielded "nan" entries for the Galactic coordinates of the 31 catalog sources and 6 reject sources within $88\rlap{.}''3$ of the north Galactic pole, and the 39 catalog sources and 5 reject sources within $87\rlap{.}''8$ of the south Galactic pole. The discrepancy in the glon and glat Galactic coordinates of sources compared to coordinates calculated using the IAU-defined system (Blaauw et al. 1960) increases with absolute Galactic latitude from < 1" in the Galactic plane to 88" near the Galactic poles. These glon and glat values (including the 81 with glat = "nan") appear in the NERSC release of the CatWISE Preliminary catalog and reject table files. In the IRSA release, these columns are hidden, and in addition the 81 glat "nan" values have been replaced with $+90°$ or $-90°$ as appropriate.

C. COMBINING ASCENDING AND DESCENDING SCAN POSITIONS

Here we provide additional details on how ascending and descending scan positions are combined for the CatWISE Preliminary Catalog. Positions are averaged using inverse-covariance weighting. The averaging is done in a local Cartesian projection consistent with the uncertainty representation.

A transformation matrix T is defined as follows: starting with a Cartesian (x, y, z) system whose z axis points to the celestial north pole and whose x axis points to the vernal equinox, we perform two Euler rotations that place the z' axis of the rotated system on the ascending celestial (α, δ) position with the y' axis aligned with the local north-south direction, and the x' axis aligned with the local east-west direction. First, rotate about the z axis by $\phi_1 = \alpha - 90°$, then rotate about the x' axis by $\phi_2 = \delta - 90°$. Then T is given by:

$$T \equiv \begin{bmatrix} T_{11} & T_{12} & T_{13} \\ T_{21} & T_{22} & T_{23} \\ T_{31} & T_{32} & T_{33} \end{bmatrix} \tag{C1}$$

with elements:

$$T_{11} = \cos\phi_1$$

$$T_{12} = \sin\phi_1$$

$$T_{13} = 0$$

$$T_{21} = -\cos\phi_2\sin\phi_1$$

$$T_{22} = \cos\phi_2\cos\phi_1 \tag{C2}$$

$$T_{23} = \sin\phi_2$$

$$T_{31} = \sin\phi_2\sin\phi_1$$

$$T_{32} = -\sin\phi_2\cos\phi_1$$

$$T_{33} = \cos\phi_2$$

This corresponds to a z' axis that looks outward from the origin, so any nearby α', δ' position will have an (x', y', z') vector in the rotated system whose z' component will be positive and close to 1. By "nearby" we mean within a few arcseconds of the origin, since it is very rare for an extracted source's position to vary between the ascending and descending solutions by more than that. This justifies our Cartesian approximation.

The coordinate system is computed for the ascending position, so that the ascending position of the source has coordinates $(0, 0, 1)$. The descending position (α', δ') is mapped into that system as follows. We construct the vector v to the descending position in the original celestial coordinate system:

$$v_1 = \cos\alpha'\cos\delta'$$

$$v_2 = \sin\alpha'\cos\delta' \tag{C3}$$

$$v_3 = \sin\delta'$$

and transform it into the new system,

$$(x', y', z') \equiv Tv \tag{C4}$$

wherein its x' and y' coordinates are the offsets of the descending position from the ascending position.

The (x', y') coordinates are averaged with $(0,0)$ using inverse covariance weighting. We construct 2×2 error covariance matrices Ω_a and Ω_d for the ascending and descending vectors using the corresponding σ_α, σ_δ, and $\sigma_{\alpha\delta}$:

$$
\begin{aligned}
\Omega_a &= \begin{bmatrix} \sigma_\alpha^2 & \sigma_{\alpha\delta}|\sigma_{\alpha\delta}| \\ \sigma_{\alpha\delta}|\sigma_{\alpha\delta}| & \sigma_\delta^2 \end{bmatrix}_a \\
\Omega_d &= \begin{bmatrix} \sigma_\alpha^2 & \sigma_{\alpha\delta}|\sigma_{\alpha\delta}| \\ \sigma_{\alpha\delta}|\sigma_{\alpha\delta}| & \sigma_\delta^2 \end{bmatrix}_d
\end{aligned}
\tag{C5}
$$

A minimum value of 10^{-8} is enforced for any zeroes on the diagonal. The merged (i.e., inverse-covariance-weighted average) vector (x_m, y_m, z_m) and associated covariance matrix are computed as follows:

$$
W_a = \Omega_a^{-1}, \quad W_d = \Omega_d^{-1}
\tag{C6}
$$

$$
\Omega = (W_a + W_d)^{-1} \equiv \begin{bmatrix} \Omega_{11} & \Omega_{12} \\ \Omega_{21} & \Omega_{22} \end{bmatrix}
\tag{C7}
$$

$$
\begin{bmatrix} x_m \\ y_m \end{bmatrix} = \Omega \left(W_a \begin{bmatrix} 0 \\ 0 \end{bmatrix} + W_d \begin{bmatrix} x' \\ y' \end{bmatrix} \right) = \Omega\, W_d \begin{bmatrix} x' \\ y' \end{bmatrix}
\tag{C8}
$$

$$
z_m = \sqrt{1 - x_m^2 - y_m^2}
$$

$$
\sigma_\alpha = \sqrt{\Omega_{11}}, \quad \sigma_\delta = \sqrt{\Omega_{22}}, \quad \sigma_{\alpha\delta} = \text{sign}(\Omega_{12})\sqrt{|\Omega_{12}|}
\tag{C9}
$$

The celestial coordinates corresponding to the (x_m, y_m, z_m) vector are obtained using the inverse of the transformation matrix T described above, which is the transpose because T is orthonormal:

$$
\begin{bmatrix} v_1' \\ v_2' \\ v_3' \end{bmatrix} \equiv \begin{bmatrix} T_{11} & T_{21} & T_{31} \\ T_{12} & T_{22} & T_{32} \\ T_{13} & T_{23} & T_{33} \end{bmatrix} \begin{bmatrix} x_m \\ y_m \\ z_m \end{bmatrix}
\tag{C10}
$$

$$\alpha_m = \tan^{-1}\left(\frac{v_2'}{v_1'}\right), \quad \delta_m = \sin^{-1} v_3' \tag{C11}$$

The image pixel coordinates are then computed for the merged position using the coadd WCS information.

REFERENCES

Ashby, M. L. N., Stanford, S. A., Brodwin, M., et al. 2013, ApJS, 209, 22.

Bakos, G. Á., Sahu, K. C., & Németh, P. 2002, ApJS, 141, 187

Bañados, E., Venemans, B. P., Mazzucchelli, C., et al. Nature, 553, 473B.

Blaauw, A., Gum, C. S., Pawsey, J. L., et al. 1960, MNRAS, 121, 123.

Brodwin, M., Stanford, S. A., Gonzalez, A. H., et al. 2013, ApJ, 779, 138.

Caselden, D., Westin, P., Meisner, A., et al. 2018, ASCL:1806.004.

Connors, M., Wiegert, P., & Veillet, C. 2011, Nature, 475, 481

Cutri, R. M., Wright, E. L., Conrow, T., et al. 2012, Explanatory Supplement to the WISE All-Sky Data Release Products, http://wise2.ipac.caltech.edu/docs/release/allsky/expsup

Cutri, R. M., Wright, E. L., Conrow, T., et al. 2013, Explanatory Supplement to the AllWISE Data Release Products, http://wise2.ipac.caltech.edu/docs/release/allwise/expsup

Cutri, R. M., Mainzer, A., Conrow, T., et al. 2015, Explanatory Supplement to the NEOWISE Data Release Products, http://wise2.ipac.caltech.edu/docs/release/neowise/expsup

Gaia Collaboration, Brown, A. G. A., Vallenari, A., et al. 2018, A&A, 616, A1

Gelino, C. R., Kirkpatrick, J. D., Cushing, M. C., et al. 2011, AJ, 142, 57

Gonzalez, A. H., Gettings, D. P., Brodwin, M., et al. 2019, ApJS, 240, 33.

Høg, E., Fabricius, C., Makarov, V. V., et al. 2000, A&A, 355, L27

Jarrett, T. H., Cohen, M., Masci, F., et al. 2011, ApJ, 735, 112

Kirkpatrick, J. D., Cushing, M. C., Gelino, C. R., et al. 2011, ApJS, 197, 19

Kirkpatrick, J. D., Schneider, A., Fajardo-Acosta, S., et al. 2014, ApJ, 783, 122

Kirkpatrick, J. D., Martin, E. C., Smart, R. L., et al. 2019, ApJS, 240, 19

Laigle, C., McCracken, H. J., Ilbert,)., et al. 2019, ApJS, 224, 24.

Lang, D. 2014, AJ, 147, 108

Lang, D., Hogg, D. W., & Schlegel, D. J. 2016, AJ, 151, 36

Lazorenko, P. F., & Sahlmann, J. 2018, A&A, 618, A111

Lindegren, L., Hernández, J., Bombrun, A., et al. 2018, A&A, 616, A2

Luhman, K. L. 2013, ApJL, 767, L1

Luhman, K. L. 2014, ApJL, 786, L18

Marsh, K. A., & Jarrett, T. H. 2012, PASA, 29, 269

Masci, F. 2013, arXiv:1301.2718

Mainzer, A., Bauer, J., Grav, T., et al. 2011, ApJ, 731, 53

Mainzer, A., Bauer, J., Cutri, R. M., et al. 2014, ApJ, 792, 30

Marocco, F., Caselden, D., Meisner, A. M., et al. 2019, ApJ, 881, 17

Marocco, F., Kirkpatrick, J. D., Meisner, A. M., et al. 2020, ApJL, 888, L19

Mauduit, J.-C., Lacy, M., Farrah, D., et al. 2012, PASP, 124, 714

Meisner, A. M., Lang, D., & Schlegel, D. J. 2018a, RNAAS, 2, 1

Meisner, A. M., Cushing, M. C., Cutri, R., et al. 2018b, RNAAS, 2, 140

Meisner, A. M., Lang, D., & Schlegel, D. J. 2018c, RNAAS, 2, 202

Meisner, A. M., Lang, D., Schlafly, E. F., et al. 2019a, PASP, 131, 124504

Meisner, A. M., Caselden, D., Kirkpatrick, J. D., et al. 2019b, ApJ, in press (arxiv:1911.12372)

Sanders, D. B., Salvato, M., Aussel, H., et al. 2007, ApJS, 172, 86

Schlafly, E. F., Meisner, A. M., & Green, G. M. 2019, ApJS, 240, 30

Scholz, R.-D. 2014, A&A, 561, A113

Skrutskie, M. F., Cutri, R. M., Stiening, R., et al. 2006, AJ, 131, 1163

Stauffer, J., Tanner, A. M., Bryden, G., et al. 2010, PASP, 122, 885

Tsai, C.-W., Eisenhardt, P. R. M., Wu, J., et al. 2015, ApJ, 805, 90

van Leeuwen, F. 2007, A&A, 474, 653

Wright, E. L., Eisenhardt, P. R. M., Mainzer, A. K., et al. 2010, AJ, 140, 1868